Chemical Geology 717 (2026) 123491

Contents lists available at ScienceDirect

Chemical Geology

journal homepage: www.elsevier.com/locate/chemgeo

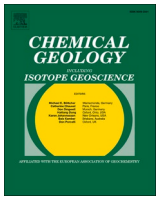

Research Paper

Kaolinite genesis and the formation of REE ion adsorption deposits

Martin Smith [a,*], Eva Marquis [a,b], Liam Hardy [a], Adrian Boyce [c], Kathryn Goodenough [d], Guillaume Estrade [e], Jindrich Kynicky [f], Cheng Xu [g]

[a] School of Applied Sciences, University of Brighton, Brighton, UK
[b] Camborne School of Mines, University of Exeter, Falmouth, UK
[c] Scottish Universities Environment Research Centre, East Kilbride, Glasgow, UK
[d] British Geological Survey, The Lyell Centre, Edinburgh, UK
[e] Laboratoire Géosciences Environnement Toulouse (GET), Université Toulouse 3 Paul Sabatier, Toulouse, France
[f] BIC Brno, Technology Innovation Transfer Chamber, Brno 61200, Czech Republic
[g] Laboratory of Orogenic Belts and Crustal Evolution, School of Earth and Space Sciences, Peking University, Beijing 100871, China

ARTICLE INFO

Editor: Marco Fiorentini

Keywords:
Ion adsorption deposit
Rare earth elements
Kaolinite
Crystallinity
Adsorption
Climate

ABSTRACT

Ion adsorption deposits (IAD), where the Rare Earth Elements (REE) occur adsorbed onto clay minerals in weathered granitoids, are a major source of the critical REE. In this study we aim to test if there is an influence from the climatic or epigenetic conditions of kaolinite formation on the potential for IAD formation. Samples were collected from logged transects from 3 sites with clay adsorbed REE (Zhaibei, China; Ambohimirahavavy, Madagascar; Monchique, Portugal) and analysed for bulk REE content and ammonium sulphate leachable REE, followed by kaolinite separation, characterisation and stable isotope analysis to determine the conditions of formation. Saprolite weathering zones are enriched in the REE relative to bedrock, with leachable fractions between 10 and 90%. Kaolinite dD and $\delta^{18}O$ indicate formation from 86 to ~20 °C. Higher mean T for Portugal and Madagascar reflects the presence of late epigenetic hydrothermal kaolinite prior to weathering. Once the effects of position in the weathering profile have been isolated using the sign and magnitude of the Ce anomaly, the % leachable REE correlates with T, with high % leachable at lower formation T. Analysis of oriented clay mounts by XRD shows that kaolinite crystallinity is variable between sites and within profiles. The variation in leachable fraction REE correlates to increased adsorption onto finer kaolinite crystallite sizes, with corresponding enhanced surface area, which in turn can be related to kaolinite formation conditions. Kaolinite crystallinity is major factor in formation of economic IAD mineralisation, alongside intensity of weathering and changing pH in soil profiles. Hydrothermal kaolinite is unfavourable for the formation of ion adsorption deposits compared to weathering kaolinite.

1. Introduction

Ion adsorption deposits are characterised by containing over 50% of the total Rare Earth Elements (REE) in an easily leachable form (Chi and Tian, 2008; Sanematsu and Watanabe, 2016; Beard et al., 2025; Russo et al., 2025). Despite accounting for only 6.5% of active REE mines and 3.5% REE projects in development, these deposits provide over 80% of the global supply of heavy REE (HREE) and contribute to LREE production (Liu et al., 2023). The REE, notably Pr, Nd and Dy, are widely classified internationally as critical resources (e.g. Mudd et al., 2024; European Union, 2024; Nassar et al., 2025), a result of supply restrictions and their importance for high strength magnets that underpin renewable energy generation and electric transportation (Ballinger et al., 2020). Synchrotron X-ray adsorption studies have demonstrated that leachable REE occur as 8 or 9 co-ordinated hydrous ions, which are adsorbed as outer sphere complexes on the surface of kaolinite and halloysite (Yamaguchi et al., 2018; Borst et al., 2020). Genetic models have focussed on the leaching of the REE from REE-minerals or REE-enriched silicates at acidic pH (~4) in the upper soil profile or at topographic elevation, and their adsorption at hydraulic or chemical (redox/pH) boundaries deeper in the system or as a result of topographically driven lateral flow (Sanematsu and Watanabe, 2016; Li et al., 2020). Experimental studies (Coppin et al., 2002; Wan and Liu, 2005, 2006; Gao et al., 2017; Villanova-de-Benavent et al., 2026) have

* Corresponding author.
E-mail address: martin.smith@brighton.ac.uk (M. Smith).

https://doi.org/10.1016/j.chemgeo.2026.123491
Received 5 September 2025; Received in revised form 5 May 2026; Accepted 13 May 2026
Available online 18 May 2026

shown, in the absence of strong ligands, kaolinite is a LREE specific adsorbent, and the formation of HREE rather than LREE enriched deposits (e.g. Zudong; Li et al., 2019) is a function of magmatic or hydrothermal pre-enrichment in the protolith (Li et al., 2019; Chaoxi et al., 2023). Villanova-de-Benavent et al. (2026) also examined the role of kaolinite crystallinity in adsorption and showed an order of magnitude (x10) increase in the mean K_d for all REE at pH 4 at 100 nm crystallite size compared to 12 nm crystallite size. This increase is of the same magnitude, or larger, than the difference in adsorption between pH 4 and pH 6 (Coppin et al., 2002; Villanova-de-Benavent et al., 2026). Therefore, REE absorption on kaolinite is a strong function of both the solution chemistry and the properties of kaolinite clay minerals in the profile. The important kaolinite properties are grain size and crystallinity plus dependent properties such as surface area, defect density and cation exchange capacity (Laveuf and Cornu, 2009; Sanematsu and Watanabe, 2016; Li and Zhou, 2023), whilst the shift from leaching to adsorption is controlled by the change in pH from 4 to 6 at shallow profile depths to 5.5 to 6.5 in lower, REE adsorption zones (Sanematsu and Watanabe, 2016; Li et al., 2022). These weathering pore fluids are distinct from deep circulating groundwater, with a pH of 8.4 at 148 m reported at the Zudong deposit (Li et al., 2019). At deposit scale, topography is a significant control on deposit formation, with leaching at topographic highs, and enhanced adsorption at lows, whilst topographically driven lateral flow may also influence the REE distribution (Estrade et al., 2019; Li et al., 2020).

Alongside S.E. Asia (Sanematsu et al., 2009; Sanematsu et al., 2013; Sanematsu et al., 2015; Mentani et al., 2010; Padrones et al., 2017; Maulana et al., 2016), ion adsorption mineralisation has now been reported from areas in North (Foley and Ayuso, 2015; Bern et al., 2017) and South America (Rocha et al., 2013; Santana et al., 2015; Pinto-Ward, 2017), Africa (Le Couteur, 2011; Estrade et al., 2019), and Europe (Hardy et al., 2016) suggesting formation under a range of climatic and weathering conditions. Deposits in southern China and neighbouring areas of SE Asia are located in subtropical regions. Most are within current temperate, dry winter, or temperate, no dry season, climatic zones according to the Köppen-Geiger classification, with some reported from Malaysia in monsoonal regions (Fig. 1; Beck et al., 2018). Those in Madagascar (Estrade et al., 2019), Malawi (Le Couteur, 2011) and Brazil (Pinto-Ward, 2017) are currently also subtropical with monsoonal or savannah type climates. Ion adsorption mineralisation has also been reported in sub-tropical, wet temperate conditions at Liberty Hill, South Carolina, USA (Bern et al., 2017), and current Mediterranean conditions with a temperate, dry summer climate at Monchique, Portugal (Hardy et al., 2016). Deposits in Australia, sometimes referred to as clay-hosted REE (Knorsch et al., 2025), are reported with a mixed mode of occurrence of the REE including detrital, smectite clay adsorbed and as authigenic carbonates (e.g. Kopparmura; Löhr et al., 2024) reflecting fluvial transport and deposition in marine or transitional environments, on karstic surfaces, at high pH (up to 8.3). The range in conditions in in-situ deposits is further complicated by the pre-weathering hydrothermal alteration of the bedrock in several deposits, meaning that clays were also potentially generated under late epithermal (150–50 °C) conditions. Given the importance of kaolinite particle properties for adsorption, it is crucial to understand the range of genetic conditions involved in the formation kaolinite within IADs; both to develop comprehensive genetic models and to guide global exploration for this critical style of mineralisation. In particular, it is vital to be able to link REE enrichment in IADs to the history of the deposit, from bedrock hydrothermal alteration to weathering under different conditions. This can be achieved by using a combination of stable isotope data and crystallinity analyses on kaolinite, to generate information about the temperatures at which those minerals formed.

In this study we have analysed the stable isotope composition, bulk and leachable REE content and crystallographic parameters of kaolinite from IADs developed across a range of environmental conditions, enabling isolation of the controls on deposit genesis relating to the conditions of weathering and the pre-mineralisation history of the protolith. Resulting data are used to develop models for IAD genesis that will help guide exploration beyond the currently exploited deposits in China and S.E. Asia.

2. Methods

2.1. Sampling

Samples were collected from logged weathering profiles at each site, either from existing drill core, hand excavated pits or exposed pit or road-cut sections, and then double bagged for transport back to the UK. Samples were subsequently stored double bagged and placed in sealed plastic boxes at 4 °C. The logs were classified using a lateritic classification of soil (the humic layer with no visible rock structure and active plant roots), pedolith (limited plant roots, no visible rock structure),

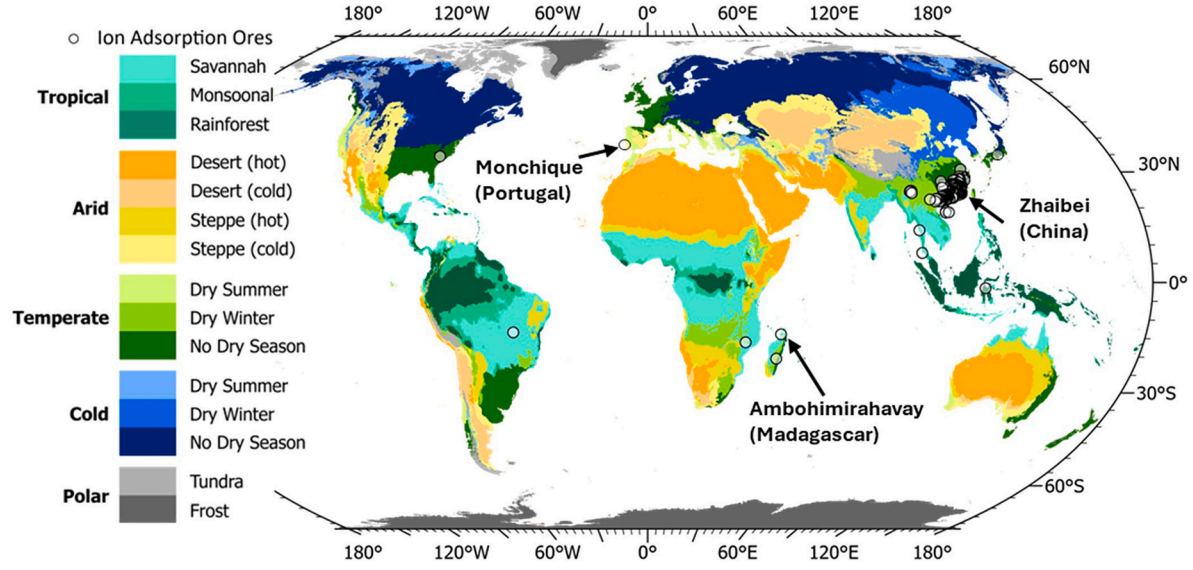

Fig. 1. World map of the Köppen-Geiger climate zones from Beck et al. (2018) showing the location of reported ion adsorption REE deposits (Beard et al., 2025), and the sites used in this study.

saprolite (dominated by soil and laterite minerals with discernible relic rock structures), and saprock (intensely weathered bedrock) (Eggleton, 2001; Taylor and Eggleton, 2001). At Monchique ferricrete was also noted (soil cemented by iron oxides and oxyhydroxides).

2.2. Bulk rock and leachable REE by ICP-MS

Bulk rock and leachable REE analyses were carried out at the University of Brighton using an Agilent 7900 ICP-MS. Bulk samples were first fused using ~0.1 g sample to 4 g lithium metaborate flux using a Fluxana induction furnace, and the resulting glass beads were dissolved in 100 mL of 10% nitric acid prior to dilution to 250 mL with deionised (18 MΩ) water. The easily leachable portion was determined by placing 1 g sample in 50 mL 0.5 M ammonium sulphate solution acidified to pH 4 using concentrated sulphuric acid, and then agitating in an end-over-end shaker for 1 h. Both sets of samples were then analysed using an collision cell reaction system operated in He mode to reduce polyatomic interferences. A multi-element calibration standard (8500–6944 Agilent) was diluted with 2% nitric acid and blank $LiBO_3$ and $(NH_4)_2SO_4$ solutions to ensure matrix matching, to calibrate the REE from 1 μg/L to 500 μg/L. Internal standard (Rh) was added via online internal standard solution addition to all standards, samples and blanks. Bulk rock analyses of certified reference materials BCR2 (basalt) and GSP2 (granodiorite) show all REE, U and Th analyses are repeatable within 5% (2), and are within 5% of certified reference values. No certified reference material exists for REE leaching experiments, but repeat analyses of BCR701 (Rauret et al., 2001) showed that leaches reproduced values within 5% precision. Analyses of surface water samples from Madagascar were carried out by ICP-MS at the British Geological Survey.

2.3. Mineralogical characterisation

Kaolinite mineral separates were obtained by suspension in deionised water with 1.5 ml Calgon© then centrifugation at 750 rpm to remove the >2 μm fraction, followed by centrifugation of the supernatant at 3000 rpm to concentrate the <2 μm fraction. The dried samples were subjected to chemical purification to remove residual carbonate (2 M sodium acetate plus 2 M acetic acid buffer solution at pH 4.8, for 2 h at a temperature of 40 °C - Gilg et al., 2004; Bergaya and Lagaly, 2013), organic matter (10% hydrogen peroxide solution at 70 °C – Girard et al., 2000) and oxides and hydroxides (0.3 M sodium citrate solution, followed by 8 ml of 1 M sodium hydrogen carbonate solution at 75 °C – Klug and Alexander, 1975). Gibbsite is not removed during the latter chemical treatment, thus heating of kaolinite separates at 200 °C was done in an attempt to remove this phase. All samples were washed with 18.2 MΩ deionised water between stages. Mineral separates were heated at 200 °C for 2 h under vacuum conditions to remove adsorbed H_2O prior to O and H gas extraction.

Kaolinite separates were examined by X-ray diffraction after centrifugation, and then before and after chemical treatment. All samples were analysed as oriented clays mounted on a glass slide. Samples from Madagascar were analysed using an X'Pert Pro MPD X-ray diffractometer (XRD) at the University of Brighton using Cu Kα X-rays generated at 40 kV and 15 nA. Samples from China and Portugal were analysed using a Rigaku Miniflex XRD at the University of Brighton, using the same analytical conditions. For both instruments the measurement interval was 0.01° 2θ The Full Width Half Maximum (FWHM) was determined on the kaolinite ~12° 2θ (7 Å) peak as a measure of kaolinite crystallinity (Mahmoud et al., 2018) and the corresponding crystallite size calculated using the Scherrer equation (Klug and Alexander, 1975). Peak broadening can be related to decrease in crystallite size, which has a strong linear relationship with the Hinkley index used to characterise structural order-disorder in kaolinite (Awad et al., 2018). Samples post-physical and chemical treatment were also analysed to check for the final mineral separate purity and any change relative to the initial kaolinite separate (Supplementary Figs. 1–4: https://doi.org/10.17033/DATA.00000335).

2.4. Stable isotope analyses

All stable isotope analysis work was undertaken at the Scottish Universities Environment Research Centre (SUERC, Glasgow). Mineral separates were analysed for O isotopes using a laser fluorination procedure, involving total sample reaction with excess ClF_3 using a CO_2 laser at temperatures in excess of 1500 °C (Sharp, 1990). Approximately 1–2 mg of sample were loaded into a platinum sample holder and evacuated to 10^{-3} mbar. After prefluorination using ClF_3, to ensure removal of all non-structurally bound O_2, samples were held under vacuum conditions for 1 h. Subsequent laser fluorination resulted in 100% release of O_2 from the silicate lattice. This O_2 was converted to CO_2 by reaction with hot graphite, which was then analysed using a VG SIRA 2 dual inlet mass spectrometer. The results are reported in standard δ notation, expressed in per mil (‰) deviations from VSMOW. Reproducibility on well characterised standards varied from 0.08 (1σ; $n = 6$) to 1.20 (1σ; $n = 4$). On standard YP2 reproducibility was 0.32 (1σ; $n = 10$) which is taken as typical for the methodology.

Hydrogen isotope analysis was done by in vacuo bulk heating following the method of Donnelly et al. (2001). Approximately 35 to 50 mg of sample were loaded into a platinum sample holder and evacuated to 10^{-3} mbar. Samples were heated using an induction coil to c. 1100 °C for 30 min. An aliquot of sample SR275 was step heated at temperature increments of 200, 250, 300, 350, 400 and 1100 °C to assess the δD of hydrogen aliquots outgassed over a range of temperatures. This was done to determine if all δD was released from structurally bound OH in kaolinite or there if was hydrogen contribution from adsorbed OH and contaminants, the results of this analysis are presented in Supplementary Table 5. Released H_2O was passed through a chromium furnace and converted to H_2. The hydrogen aliquots were analysed using a VG OPTIMA dual inlet mass spectrometer. The results are given in standard δ notation, expressed in per mil (‰) deviations from VSMOW. Reproducibility on well characterised standards varied form 0.71 (1σ; $n = 2$) to 2.51 (1σ; $n = 5$).

Water samples were collected from stream and river drainage across the Ambohimirahavavy Complex Area, and in one instance from shallow groundwater that accumulated in a sampling pit. Pore water samples were collected from the soil profiles at Monchqiue using MacroRhizons (Dickens et al., 2007). The water sampleswere analysed for $\delta^{18}O$ and δD to provide an indication of meteoric and pore water isotope compositions.

3. Results

The full data set from this study is available at https://doi.org/10.17033/DATA.00000334.

3.1. Site characterisation

Samples used in this study were collected from the Zhaibei granite, China (Wang et al., 2015; Borst et al., 2020), the Ambohimirahavavy alkaline complex, Madagascar (Estrade et al., 2019), and the Monchique syenite, Portugal (Rock, 1974). Key geological and climatic characteristics of the sites are summarised in Table 1.

The Zhaibei granite samples were taken from a 12 m thick laterite profile developed on biotite syeno-granite (Fig. 2a; Wang et al., 2015; Zhao et al., 2022). The Köppen-Geiger class for this site is humid subtropical, no dry season (Cfa; Beck et al., 2018). Mean annual temperatures are 19 °C, with total annual rainfall of ~1600 mm reported at Ganzhou (Zhao et al., 2022; Weather and Climate, 2026). The granite has a topographic variation of 300 to 800 m, with weathering crusts developed across the area on slopes between 20 and 35° (Zhao et al., 2022). The area is drained by a dendritic river system and is heavily wooded except for where denuded by agricultural and urban

Table 1
Locations and climatic conditions of the study sites.

Study site		Zhaibei	Ambohimirahavay	Monchique
Weather Station*		Ganzhou	Ambanja	Monchique
Country		China	Madagascar	Portugal
Study site location	**Latitude**	24°54′40.89″N	13°49′0.71″S	37°19′2.97″N
	Longitude	115° 8′36.18″E	48°10′56.68″E	8°34′6.96″W
Bedrock		Biotite syeno-granite	Syenite/peralkaline granite	Syenite
Köppen-Geiger class		Temperate, no dry season	Tropical, monsoon	Temperate, dry summer
Monthly Mean Temperature (°C)*	**Peak**	32.8	28.8	27.8
	Range	5.3–32.8	22.2–28.8	9.2–27.8
Monthly Mean Rainfall (mm)*	**Peak**	239	417	25
	@Peak T#	131	417	1
	Range	33–239	22–417	1–25

*Weather Atlas (2026).
#@Peak T - Rainfall at peak temperature.

development in valley bottoms and around some IAD workings (Fig. 2b).

The Ambohimirahavavy samples are taken from 2 boreholes and 3 hand dug pits across the margin of the alkaline ring complex (Fig. 2c). Borehole 1 (BH1; samples SR211-SR246) intersected a 12 m thick laterite profile overlying syenite with alkali pegmatite dykes (Estrade et al., 2019) with samples taken from 2 to 12 m deep in saprolite and saprock. The Köppen-Geiger class for this site is Tropical highland, temperate with dry winters (Cwb; Beck et al., 2018). Mean annual temperature is 25.6 °C, with total annual rainfall of ~1600 mm recorded at Ambanja (Weather and Climate, 2026). The syenitic ring dyke forms an annular topographic high with approximately 400 m peak elevation relative to sea level, with a central caldera floor at ~200 m and a central rhyolite dome rising to 300 m. Drainage is radial on the flanks of the ring dyke, whilst the central caldera is drained via streams breaching the topographic high. The area is heavily vegetated with secondary growth rainforest after slash and burn agriculture (Fig. 2d). Rare earth element mineralised weathering profiles are developed on the central rhyolite dome and, more significantly on the seaward slope of the ring dyke (Estrade et al., 2019) with slopes of ~16°. The profiles sampled in this study (Fig. 2c, d) include hand dug pits on the rhyolite dome (Pit 2), the crest of the syenite ring dyke (Pit 3) and above the REE-mineralised peralkaline dykes on the seaward slope (Pit 4). Two boreholes from the seaward slope were also sampled (BH1 – TAND44; BH2 – TAND97). The profiles typically consist of ~90 cm of gibbsite-kaolinite pedolith with active plant roots, overlying a lower kaolinite/halloysite dominant pedolith and saprolite of variable thickness (3-12 m). The lower saprolite and upper saprock show increasing contents of relict alkali felspar, and in some cases minor quartz. Goethite is a minor component of the laterite (Estrade et al., 2019).

The Monchique samples were taken from 2 laterite profiles, one 7 m and one 4 m thick developed on syenite (Fig. 2e). The Köppen-Geiger class for this site is mediterranean, dry summer (Csa; Beck et al., 2018). Mean annual temperature is 18 °C, with total annual rainfall of 258 mm recorded at Monchique town (Weather and Climate, 2026), but upto 1000 mm per annum at higher elevation (Hoque et al., 2024). The Monchique syenite forms a liner massif, with a highest elevation of 902 m, and an average of 402 m. The drainage system is radial from the syenite massif, with cold springs rising on syenite in relation to the base of weathering profiles, faults and some valley fill aquifers (Hoque et al., 2024). The area has natural vegetation of heathland and indigenous woodland, that in significant areas has been replaced with eucalyptus, pine and acacia plantations (Fig. 2f; A Rocha, 2026) the roots of which disrupt the weathering profiles. Geothermal springs rise in the western area of the massif, with surface temperatures up to 31 °C (Hoque et al., 2024). The weathering profiles sampled are close to the western contact of the syenite. Profile 3PS-11 is developed on nepheline syenite and has a maximum thickness of approximately 12 m, consisting of 15 cm of topsoil. The soil and upper saprolite consist of gibbsite and kaolinite group minerals, with increasing relict feldspar from ~50 cm deep and trace goethite throughout. The sampled profiles occur on slopes of ~14°. Profile D2B is developed on nepheline syenite cut by lamprophye and alkali basalt dykes. The general mineralogy of the profile is similar to 3PS-11, but with development of oxisol/ferricrete at 20–50 cm below surface. There is no evidence of clasts in this zone so it is inferred to be in-situ and the result of leaching and oxidation during alternating wet and dry periods.

Peak monthly average temperatures for all three sites are similar (27.8–29.5 °C). However, there are significant differences in the coincidence of peak rainfall and temperature. At both Zhaibei and Ambohimirahavavy, the peak monthly rainfall, of 223 mm and 417 mm respectively, corresponds to the monthly peak temperature. At the Monchique the maximum monthly rainfall of 25 mm corresponds with the winter minimum average temperature of 1 °C (all climate data are 30-year averages from https://www.weather-atlas.com/.).

3.2. Bulk and leachable REE

Results of bulk sample REE analyses are presented in Figs. 3–5 and Tables 2 and 3. Some data from Ambohimirahavavy, Madagascar, have been previously presented in Estrade et al. (2019). All profiles from all sites show zones of REE enrichment within the regolith profile. Within the Zhaibei granite the total REE ranges from ~200–1500 mg/kg, with the highest levels in the upper pedolith zone, but the % leachable fraction is consistently between 50 and 70% (Fig. 3). The Ce anomaly ((Ce/Ce* = Ce_{CN}/((La_{CN} + Pr_{CN})*0.5) where the subscript CN refers to the chondrite normalised (Sun and McDonough, 1989 concentration) is uniformly negative (Ce/Ce* < 1) except for in a single sample at the saprolite/saprock boundary which shows a slight positive anomaly (Ce/Ce* > 1). Profiles at Ambohimirahavavy are complicated by bedrock heterogeneity (Estrade et al., 2019), with the total REE typically ranging from ~500–2600 mg/kg, with one exceptional sample reaching 5810 mg/kg. The latter sample shows a positive Ce anomaly and hence a high contribution to total REEs is from Ce, this sample also corresponds to the inferred position of a peralkaline granite dyke within the protolith. The peak in total REE corresponds to the lowest leachable percentage in the profile, explained by the hosting of the elevated REE contents in insoluble zirconosilicates in this protolith lithology. More generally across the profiles, leachable % REE ranges from 6% to 72%, with the lowest values corresponding to samples taken from an extensively leached soil zone within a profile taken at a topographic high (Pit 3; Estrade et al., 2019) or the horizon inferred to represent a weathered peralkaline granite dyke. Highest leachable % are at the pedolith/saprolite boundary – that is at changes in the profile hydraulic properties that may retain water in the wet season. Generation of positive Ce/Ce* is most marked in the leached soil zones. At Monchique, total REE contents vary from ~400–1200 mg/kg. The highest concentrations occur at the base of the soil zone, also corresponding to the highest % leachable (73–74%), with values as low as 10–20% elsewhere in the profiles. The Ce anomaly is positive in the Fe oxide cemented layer (ferricrete) and close to the saprolite/saprock boundary, both also corresponding to low % leachable

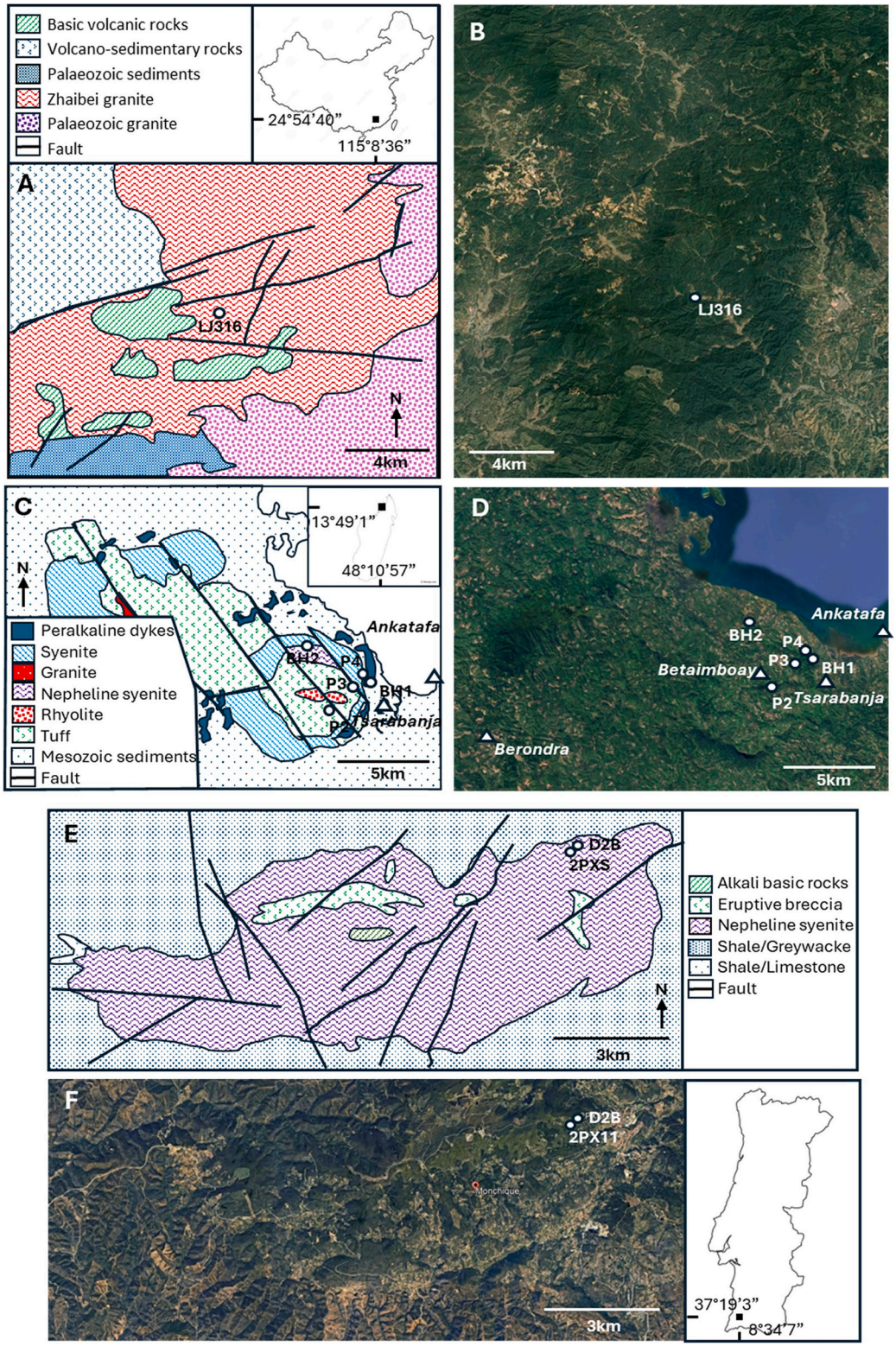

Fig. 2. Simpified geological maps and satellite imagery of each study site. (a), (b) The Zhaibei granite, China (adapted from Wang et al., 2015). (c), (d) The Ambohimirahavavy alkaline complex, Madagascar (adapted from Estrade et al., 2019). (e), (f) The Monchique syenite, Portugal (Barbosa et al., 2022). Satellite imagery from Google Earth (2026). Circles indicate sampled profiles, triangles indicate surface water samples.

REE.

Chondrite normalised REE patterns for bulk rock and ammonium sulphate leaches are shown in Fig. 4, and the percentage leached of individual REE in Fig. 5. Bedrock/Protolith granitoids for all samples are relatively light (L)REE-rich, with flat heavy (H)REE patterns and variable development of a negative Eu-anomaly. For all regolith samples, chondrite normalised patterns mirror the bedrock REE patterns, except for Ce that has either a positive or negative anomaly. Ammonium sulphate leaches show very similar patterns, but at lower absolute concentration reflecting the variation in leachable proportions. In

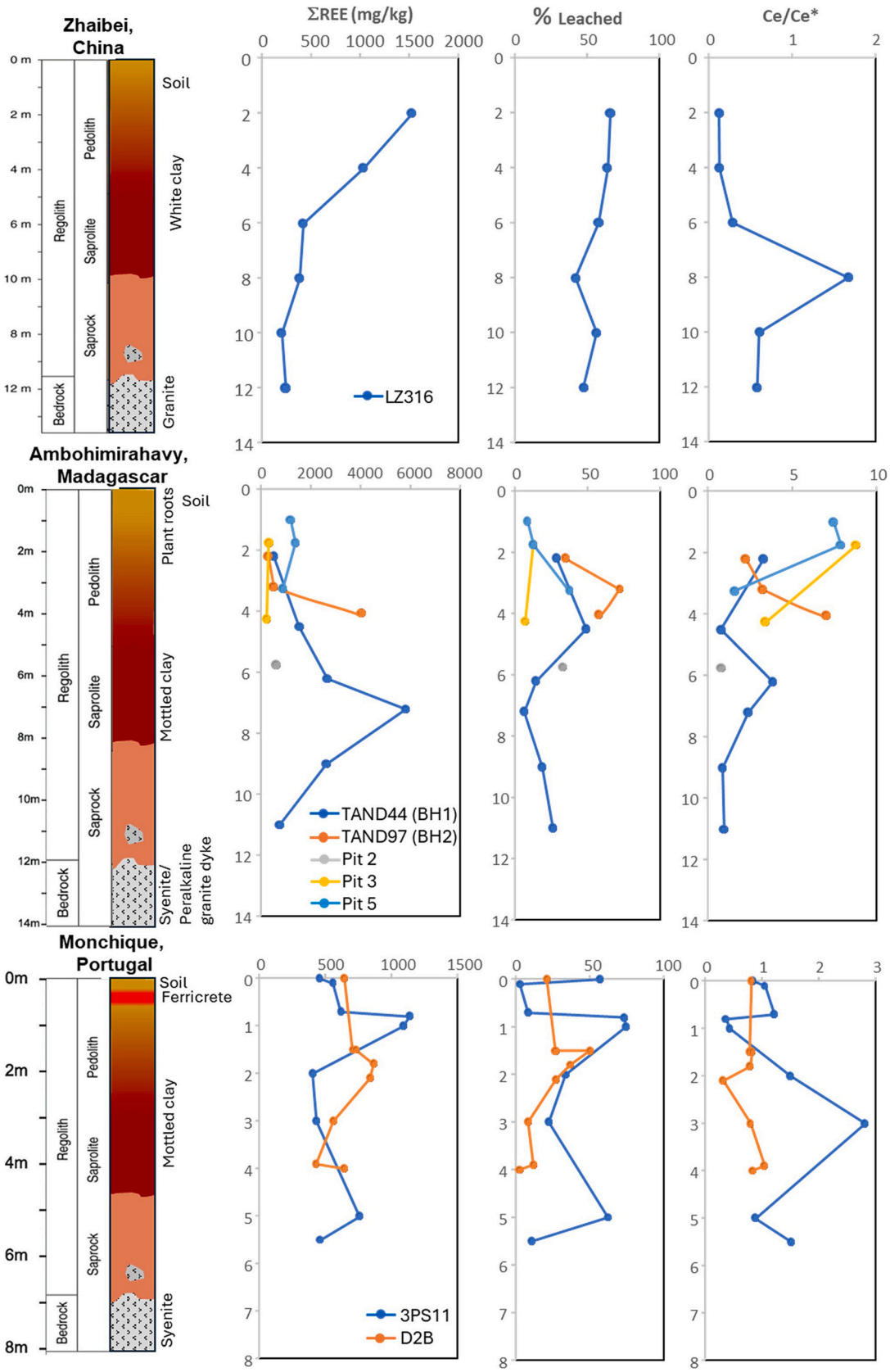

Fig. 3. Schematic logs and REE geochemistry of the weathering profiles sampled. Depth profiles show total REE in bulk digestions, % leached by ammonium sulphate solution and the Ce anomaly in the bulk digestion composition. Multiple profiles were sampled in Madagascar and Portugal.

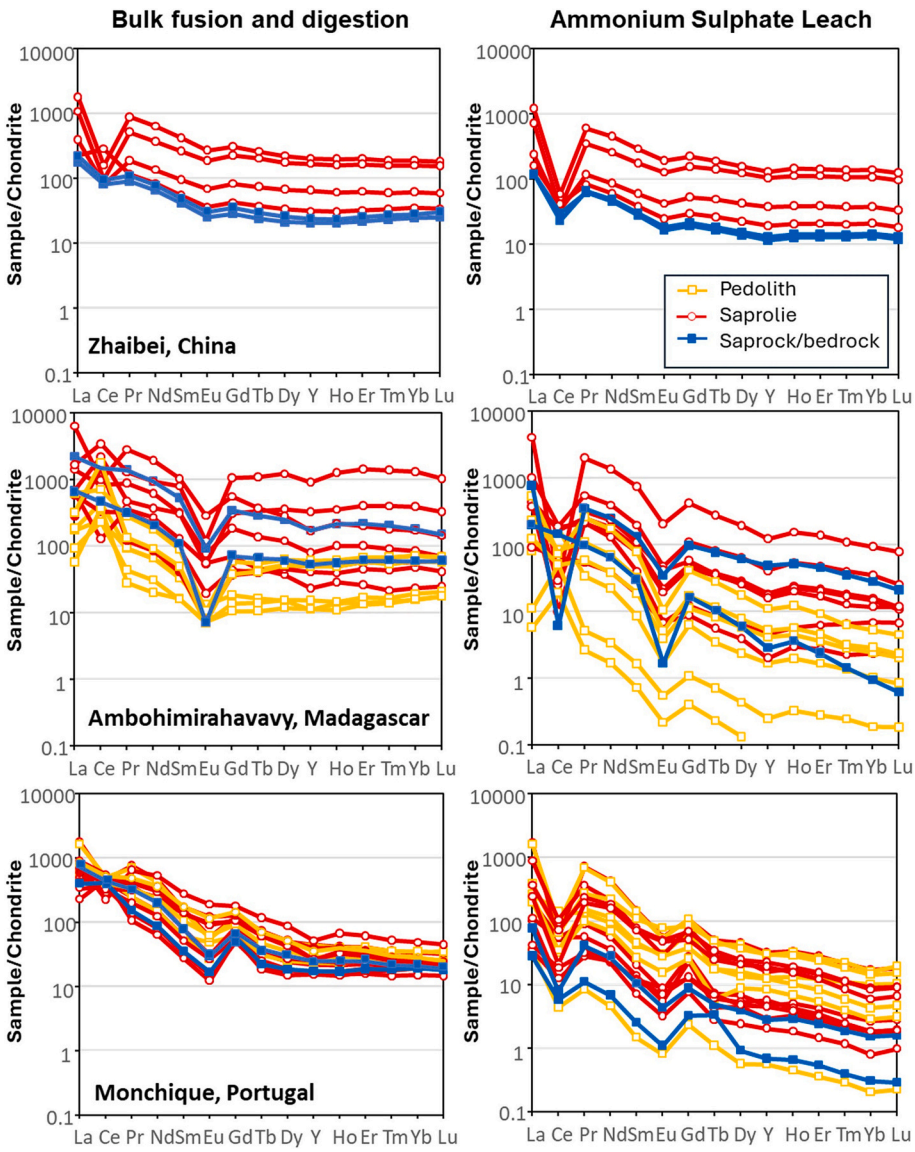

Fig. 4. Chondrite normalised REE patterns for bulk fusion and digestion and pH 4 ammonium sulphate leach from each study site.

samples from the Zhaibei granite (Fig. 5a) the leachable percentage is consistently between 50 and 70% except for Ce. This reflects the consistent development of the weathering profile with depth and the dominant form of the REE being clay adsorbed within regolith profiles, alongside the oxidation of Ce and its sequestration into insoluble oxides (cerianite - CeO_2; e.g. Sanematsu and Watanabe, 2016; Estrade et al., 2019, Li et al., 2019). At Ambohimirahavavy the range in individual REE leached varies in relation to the extent of weathering and kaolinite generation, and there is a marked contrast between LREE and HREE behaviour. This relates to the variation in REE-host minerals, with widespread mobilisation of the LREE and preferential retention of HREE in zircon and other zirconosilicates (Estrade et al., 2019; Marquis et al., 2023). Samples from Monchique show a similar pattern to Ambohimirahavavy, but with a less marked variation between LREE and HREE.

3.3. Kaolinite and clay mineralogy

In the untreated clay separate samples illite was present as a minor phase in the Zhaibei and Ambohimirahavavy samples (Fig. 6), whilst minor chlorite was present in the Monchique samples. The repeated centrifugation alongside chemical purification served to make kaolinite the dominant phase in all separates. Illite remained as a minor phase in the samples from the D2B profile from Monchique, but there is no significant difference in the reported $\delta^{18}O$ between the two profiles from Monchique, indicating the analysed signature was dominated by kaolinite (Table 4).

Fig. 6 shows XRD data for the pre-treatment clay concentrates from 5 to 15° 2θ from each site, focussed on the kaolinite ~12° 2θ diffraction peak, and data is summarised in Table 4. In the Chinese samples the full width at half maximum peak height (FWHM) varies systematically with depth from 1.01° at 2 m to 2.43° at 12 m, corresponding to a decline in crystallite size from 8.26 to 3.44 nm. In the Ambohimirahavavy samples FWHM is generally consistent throughout profiles, with a decline with depth towards the interface with bedrock from 1.41 to 0.14°, corresponding to a change in crystallite size from 5.9 to 61.4 nm. In the Monchique samples FWHM is consistently in the range 0.59 to 0.81°, corresponding to a crystallite size of 15.15 to 10.31 nm. There are mid-profile excursions to values between 0.93 and 2.10°, corresponding to a crystallite size of 8.97 to 3.97 nm. It should be noted that, assuming no lattice strain or defects, the crystallite size calculated with the Scherrer equation is applicable to the coherently scattering domain size (Hassanzadeh-Tabrizi, 2023). As such, crystallite size represents the crystalline sub-grain size, not the clay particle size. However, this measurement is relatable to the structural disorder, reactive surface

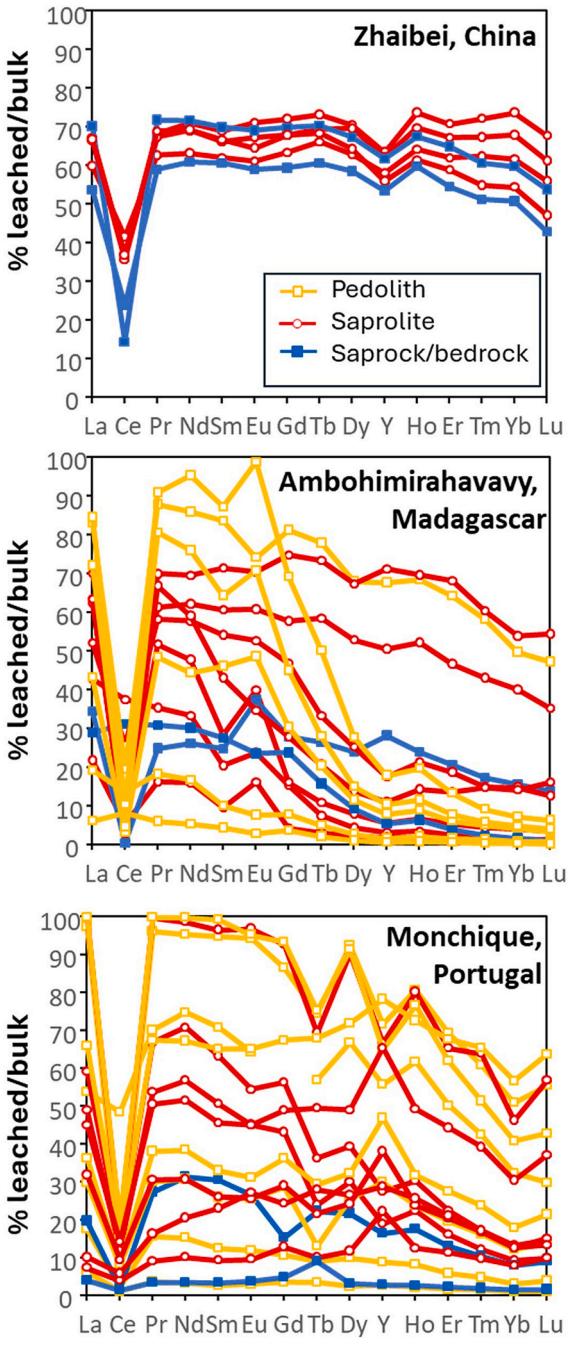

Fig. 5. The percentage leached by ammonium sulphate at pH 4 for each REE from each study site.

area, and hence number of adsorption sites per unit mass.

3.4. Stable isotope composition

The stable isotope composition of kaolinite from the 3 sites is shown in Table 5 and summarised in Fig. 7. Kaolinite $\delta^{18}O$ varies from 15.9 to 18.5‰, at Zhaibei, 13.5 to 21.5‰ at Ambohimirahavavy, and 15.6 to 23.7‰ at Monchique. Kaolinite dD varies from −62.9 to 34.1‰ at Zhaibei, from −57.6 to −24.7‰ at Ambohimirahavavy, and from −60.0 to −49.0‰ at Monchique.

Comparison of the sample composition for those samples with corresponding $\delta^{18}O$ and dD analyses with contours of kaolinite formation temperature based on the global meteoric water line (GNIP, 2024) and the fraction factors of Sheppard and Gilg (1996) suggests the majority of kaolinite formed in the range 20–50 °C, but the total range of kaolinite $\delta^{18}O$ implies a wider range of formation temperature (Fig. 8). At Zhaibei apparent temperatures range from 24 to 37 °C with a mean of 30 °C. At Ambohimirahavavy apparent temperatures range from 21 to 86 °C, with a mean of 39 °C. At Monchique apparent temperatures range from 25 to 73 °C. with a mean of 44 °C. At Ambohimirahavavy there is an increase in apparent temperature with depth, whilst at Monchique there is an apparent decrease (Table 5).

Analyses of a single bedrock clay fraction from Monchique, dominated by illite, gave a $\delta^{18}O$ of 7.2‰, which is distinct from kaolinite and indicates minimal contamination of the final kaolinite separates by illite. Lawrence and Taylor Jr. (1972) noted that illite showed no isotopic change relative to parent rocks in weathering profiles. Equally, calculation of the composition of gibbsite in equilibrium with meteoric water between 20 and 50 °C (Savin and Epstein, 1970; Vitali et al., 2001) suggests that gibbsite would have a $\delta^{18}O$ between 5 and 10‰, thus gibbsite contamination in the separates can be effectively ruled out.

3.5. Water composition

Water sampling was possible from surface water sources and shallow (<5 m) groundwater at Ambohimirahavavy and from pore fluids at Monchique (Table 5). At Ambohimirahavavy surface water $\delta^{18}O$ varied from −2.9 to −4.6‰, and dD varied from −22.4 to −13.2‰. Corresponding pH varied from 6.81 to 8.15, whilst total REE concentrations varied from 0.1 to 11.2 μg/L. At Monchique $\delta^{18}O$ varied from −2.3 to 0.1‰ and dD varied from −7.1 to 6.0‰. No water samples were recovered from the Zhaibei granite site; however, Liu et al. (2014) compiled the stable isotope composition of precipitation across southeast China. Regional precipitation from relevant stations dD varies from −45 to −25.9‰ and $\delta^{18}O$ varies from −6.9 to −4.5‰. These are shown in Fig. 7 for reference. The variation in water composition mirrors the global meteoric water line, and inter-site variation is controlled by climate, altitude and the difference between coastal (Monchique, Madagascar) continental (China) settings.

4. Discussion

4.1. Genetic conditions of kaolinite

As shown in Fig. 8, the fractionation in $\delta^{18}O$ and dD implies most kaolinite sampled equilibrated with meteoric water from 25 to 35 °C, but a significant portion equilibrated from 40 to >50 °C, notably at Ambohimirahavavy and Monchique. Calculation of the equilibration temperatures of individual kaolinite samples based on $\delta^{18}O$ of minerals and the mean water $\delta^{18}O$ from each site confirms the dominant equilibration T from 25 to 35 °C (Fig. 8); with higher temperature equilibration for some samples from Madagascar and Portugal (upto 86 °C). The mean temperatures are 30 ± 5 °C in China, 39 ± 16 °C in Madagascar and 44 ± 12 °C in Portugal. Use of maximum and minimum precipitation, surface or pore water $\delta^{18}O$ indicates a sensitivity of ~ ± 5 °C in the temperature estimates and does not remove the bias to higher temperatures seen in the Monchique samples.

Hoque et al. (2024) detected 2 dominant groundwater discharge types within the Monchique syenite – thermal waters discharging at 23–31 °C, and cooler springs discharging at 15 to 21 °C. Thermal waters were inferred to arise through deep fracture-controlled flow, with residence times up to 5000 years, whilst the cooler springs were inferred to arise from shallow, rapid flow through the regolith profile. At Monchique $\delta^{18}O$ of pore waters measured here varied from −2.3 to 0.1‰, and dD varied from −7.1 to 6.0‰. Geothermal spring water has a composition of $\delta^{18}O$ ~ -4.8‰ and dD ~ -21‰ whilst cold water springs range from $\delta^{18}O$ -4.8 to 4.0‰ and dD -15 to-24‰ (Hoque et al., 2024). Higher values reported here likely reflect the sampling of these waters during the summer season. Use of the spring water $\delta^{18}O$ values would remove the overall bias to higher temperatures in the Monchique

Table 2
Bulk rock ($LiBO_3$ fusion and nitric acid digestion) REE concentrations of the studied samples.

Bulk rock	Borehole	Depth (m)	Sc (mg/Kg)	La	Ce	Pr	Nd	Sm	Eu	Gd	Tb	Dy	Y	Ho	Er	Tm	Yb	Lu
Zhaibei, China																		
LZ316_2m		2.0	4.1	429.5	98.2	83.2	293.4	62.6	15.4	61.9	9.4	54.9	322.9	10.9	32.5	4.7	30.7	4.5
LZ316_4m		4.0	3.7	256.7	60.5	48.5	171.3	39.6	10.7	45.9	7.5	43.7	267.8	8.8	26.8	4.0	25.9	3.9
LZ316_6m		6.0	3.1	94.5	50.6	17.7	62.7	14.3	3.9	16.7	2.7	16.7	102.9	3.4	10.2	1.5	10.0	1.5
LZ316_8m		8.0	3.1	54.4	177.1	10.8	38.4	8.1	2.0	8.5	1.4	8.3	49.4	1.7	5.1	0.8	5.7	0.8
LZ316_10m		10.0	2.7	42.5	49.7	8.4	29.9	6.1	1.4	5.6	0.9	5.3	32.2	1.1	3.5	0.6	4.0	0.6
LZ316_12m		12.0	3.0	52.4	58.7	10.3	36.4	7.3	1.7	7.1	1.1	6.5	38.1	1.3	4.2	0.7	4.6	0.8
Ambohimirahavavy, Madagascar																		
SR211	TAND44	2.3	14.7	44.4	284.0	8.9	30.2	6.2	0.4	8.2	1.7	13.3	85.0	3.1	10.8	1.7	12.0	1.7
Sr219	TAND44	4.5	19.3	340.7	520.5	82.9	289.6	47.7	4.3	37.6	5.1	29.8	126.7	5.6	16.4	2.3	13.9	1.8
SR227	TAND44	6.3	36.9	165.0	1374.3	44.7	172.8	46.6	3.1	61.9	12.3	88.6	520.8	19.6	65.3	10.0	63.4	8.1
SR231	TAND44	7.3	65.2	401.0	2154.4	121.0	430.9	119.1	6.8	213.2	39.9	305.6	1441.3	69.7	232.0	34.4	215.0	25.8
SR238	TAND44	9.0	4.3	533.6	929.9	130.3	435.8	79.2	5.3	69.5	10.5	62.2	271.5	11.9	35.0	5.0	29.0	3.7
SR246	TAND44	12.0	3.6	162.8	285.2	29.9	98.4	16.3	0.4	14.1	2.4	15.6	83.1	3.1	9.6	1.5	9.6	1.5
SR275(276)	TAND97	2.3	NA	41.9	155.2	8.6	30.9	5.0	0.7	3.7	0.6	3.8	17.8	0.8	2.3	0.4	2.6	0.4
SR279(280)	TAND97	3.3	NA	154.9	79.4	33.6	125.4	19.3	3.2	14.2	1.7	9.3	37.3	1.6	4.2	0.5	3.8	0.6
SR306	TAND 109	3.75	NA	1519.8	610.0	265.2	901.4	156.1	16.4	111.9	13.6	70.9	269.9	12.1	32.4	4.5	27.9	3.6
SR573 (576)	PIT 2	5.8	NA	139.2	202.8	30.2	100.3	13.6	1.1	8.7	1.5	11.2	64.4	2.2	7.3	1.1	7.8	1.0
SR586 (584)	PIT 3	1.8	NA	13.7	230.9	2.6	9.2	2.4	0.4	2.7	0.5	3.9	24.2	0.8	2.7	0.4	3.1	0.5
SR597	PIT 3	4.8	NA	22.1	141.5	4.1	14.3	2.4	0.4	2.2	0.4	2.9	18.2	0.6	2.2	0.4	2.6	0.4
SR611	PIT 5	1.0	NA	67.9	925.0	11.2	39.2	6.1	0.5	7.4	1.5	12.3	81.8	2.7	9.4	1.4	9.4	1.5
SR617 (615)	PIT 5	2.0	NA	76.6	1105.4	12.6	42.2	7.4	0.4	7.6	1.5	12.8	78.9	2.7	9.4	1.3	9.6	1.4
SR624	PIT 5	3.3	NA	150.2	435.5	26.6	83.5	13.4	0.6	11.9	2.0	15.6	96.1	3.4	11.0	1.7	11.7	1.7
Monchique, Portugal																		
3PS-11-OX		0.0	22.9	119.5	180.5	17.9	58.7	8.9	2.7	12.0	1.1	6.0	37.1	1.2	4.0	0.7	5.2	0.9
3PS-11-TS		0.1	17.1	133.2	260.2	22.8	67.3	8.8	1.6	13.7	1.2	5.9	34.2	1.2	3.6	0.5	3.8	0.6
3PS-11-70		0.7	11.5	137.8	308.9	23.0	67.2	8.7	1.5	14.6	1.1	6.2	37.1	1.3	4.1	0.6	4.3	0.6
3PS-11-80		0.8	11.9	422.2	282.4	70.1	208.1	23.4	3.4	24.5	2.5	12.3	71.0	2.3	6.6	0.9	5.5	0.8
3PS-11–100		1.0	12.0	383.3	304.5	64.4	190.9	21.8	3.2	23.5	2.3	11.6	68.5	2.2	6.5	0.9	5.7	0.8
3PS-11-200		2.0	8.3	80.2	218.6	12.7	36.6	4.9	0.8	9.9	0.7	4.3	27.0	0.9	3.1	0.5	3.3	0.5
3PS-11-300		3.0	10.0	54.3	288.9	9.8	29.0	4.1	0.7	10.7	0.7	3.7	24.4	0.8	2.8	0.4	3.1	0.5
3PS-11-500		5.0	11.3	210.0	335.1	32.8	95.0	11.3	1.7	16.5	1.3	6.7	39.1	1.3	3.8	0.5	3.6	0.5
3PS-11-550		5.5	9.5	93.9	255.1	14.1	39.3	5.2	0.9	11.6	0.8	4.5	27.1	0.9	3.0	0.5	3.1	0.4
D2B-TS		0.1	24.4	156.6	248.4	31.2	104.8	15.3	3.5	18.3	1.7	8.7	44.8	1.6	4.5	0.6	3.9	0.6
D2B-150 A		1.5	46.3	159.9	258.0	37.8	136.6	20.6	5.1	21.2	2.2	10.4	42.0	1.8	4.8	0.6	3.9	0.5
D2B-150B		1.6	47.3	139.5	252.3	38.0	151.9	25.2	6.8	25.4	2.6	12.7	62.2	2.2	5.7	0.7	4.2	0.6
D2B-180		1.8	38.7	196.5	316.4	44.3	164.5	25.4	6.4	28.4	2.5	12.5	54.9	2.1	5.7	0.7	4.5	0.6
D2B-210		2.1	38.1	182.7	137.6	59.5	240.8	40.8	10.6	35.5	4.2	21.5	80.8	3.6	9.8	1.3	7.8	1.1
D2B-300		3.0	40.1	116.0	196.1	29.2	108.9	19.6	5.4	20.0	2.2	11.3	40.8	1.9	4.9	0.6	3.6	0.5
D2B-390		3.9	13.8	99.8	198.1	18.3	56.5	7.6	1.5	11.0	0.9	4.5	25.1	0.8	2.5	0.4	2.4	0.4
D2B-BR		5.0	10.2	170.9	267.6	30.0	90.7	11.5	1.7	13.8	1.4	7.3	38.9	1.4	3.9	0.5	3.3	0.5

NA - not analysed.

Table 3
Ammonium Sulphate leachable REE concentrations from the studies samples.

$(NH_4)_2SO_4$	Borehole	Depth	Sc	La	Ce	Pr	Nd	Sm	Eu	Gd	Tb	Dy	Y	Ho	Er	Tm	Yb	Lu
Leach		(m)	(mg/Kg)															
Zhaibei, China																		
LZ316_2m		2.0	0.07	289.2	36.2	56.9	208.7	43.2	11.0	44.7	6.92	38.8	205.1	8.07	23.02	3.39	22.63	3.08
LZ316_4m		4.0	0.05	170.4	21.6	32.7	118.4	26.2	7.2	31.2	5.19	30.5	166.6	6.17	18.02	2.67	17.63	2.38
LZ316_6m		6.0	0.03	56.6	21.0	11.1	39.6	8.9	2.4	10.6	1.79	10.5	59.8	2.15	6.32	0.93	6.17	0.82
LZ316_8m		8.0	0.03	38.2	25.4	7.7	27.5	5.6	1.4	5.9	0.95	5.6	30.5	1.13	3.33	0.50	3.38	0.45
LZ316_10m		10.0	0.02	28.4	18.3	5.8	20.7	4.1	0.9	3.8	0.59	3.4	18.0	0.69	2.04	0.31	2.16	0.29
LZ316_12m		12.0	0.02	28.1	14.0	6.1	22.1	4.4	1.0	4.2	0.66	3.8	20.4	0.77	2.26	0.35	2.33	0.32
Ambohimirahavavy, Madagascar																		
SR211	TAND44	2.3	0.10	19.0	106.4	3.2	10.1	1.3	0.1	1.3	0.12	0.58	2.65	0.11	0.27	0.03	0.16	0.02
Sr219	TAND44	4.5	0.56	238.7	115.3	50.8	179.9	28.9	2.6	21.7	2.97	15.75	64.02	2.92	7.65	0.98	5.57	0.62
SR227	TAND44	6.3	0.31	102.9	100.1	23.1	82.5	13.2	1.2	9.9	1.34	7.03	28.88	1.31	3.44	0.45	2.53	0.28
SR231	TAND44	7.3	0.34	87.2	114.1	19.7	69.1	11.4	1.1	9.0	1.24	6.62	27.91	1.23	3.25	0.42	2.38	0.26
SR238	TAND44	9.0	0.00	183.3	3.8	32.3	113.9	19.6	2.0	19.4	2.78	14.88	76.27	2.84	7.21	0.87	4.52	0.51
SR246	TAND44	12.0	0.03	46.9	88.6	9.2	29.6	4.5	0.1	3.3	0.38	1.45	4.44	0.20	0.38	0.04	0.15	0.02
SR275(276)	TAND97	2.3	0.20	21.8	39.9	5.0	17.9	2.7	0.4	1.7	0.20	0.96	3.14	0.16	0.44	0.06	0.38	0.06
SR279(280)	TAND97	3.3	0.04	128.9	15.4	29.5	107.8	16.1	2.4	11.5	1.32	6.29	25.24	1.10	2.71	0.31	1.91	0.29
SR306	TAND 109	3.75	0.10	964.5	18.0	185.5	626.8	111.4	11.5	83.6	9.97	47.73	191.98	8.42	22.06	2.73	15.01	1.93
SR573 (576)	PIT 2	5.8	NA	88.2	6.1	20.2	59.2	5.9	0.4	2.4	0.30	1.55	7.11	0.31	1.00	0.16	1.10	0.17
SR586 (584)	PIT 3	1.8	NA	2.6	31.5	0.5	1.5	0.2	0.0	0.2	0.03	0.11	0.39	0.02	0.04	0.01	0.03	0.00
SR597	PIT 3	4.8	NA	1.4	11.8	0.2	0.8	0.1	0.0	0.1	0.01	0.03	0.11	0.01	0.01	0.00	0.01	0.00
SR611	PIT 5	1.0	NA	29.3	30.4	5.4	17.4	2.8	0.2	2.2	0.30	1.42	6.50	0.24	0.57	0.07	0.39	0.05
SR617 (615)	PIT 5	2.0	NA	55.2	51.5	10.2	32.1	4.8	0.3	3.4	0.42	1.92	8.22	0.31	0.73	0.08	0.47	0.06
SR624	PIT 5	3.3	NA	127.0	44.7	24.2	79.6	11.7	0.6	8.2	1.01	4.33	17.22	0.67	1.47	0.16	0.85	0.11
Monchique, Portugal																		
3PS-11-OX		0.0	0.16	64.2	87.4	12.6	44.0	6.3	1.7	13.5	0.65	4.0	20.69	0.7	2.0	0.3	1.7	0.3
3PS-11-TS		0.1	0.02	8.1	2.7	0.8	2.1	0.2	0.0	0.5	0.0	0.1	0.90	0.0	0.1	0.0	0.0	0.0
3PS-11-70		0.7	0.05	24.2	6.8	3.6	10.2	1.1	0.2	1.6	0.1	0.6	3.28	0.1	0.2	0.0	0.1	0.0
3PS-11-80		0.8	0.03	412.0	33.7	67.5	198.6	22.2	3.2	21.2	1.8	11.4	50.95	1.9	4.6	0.5	2.8	0.4
3PS-11–100		1.0	0.16	386.3	55.9	64.4	188.6	21.1	3.1	21.8	1.6	10.5	45.79	1.8	4.2	0.6	2.6	0.5
3PS-11-200		2.0	0.03	47.5	33.8	8.5	26.0	3.1	0.5	5.6	0.3	1.7	7.45	0.3	0.7	0.1	0.4	0.1
3PS-11-300		3.0	0.04	26.6	34.5	5.3	16.5	2.1	0.3	4.7	0.2	1.1	4.62	0.2	0.5	0.1	0.3	0.0
3PS-11-500		5.0	0.08	209.9	64.8	33.6	98.3	11.3	1.7	15.5	1.0	6.1	25.44	1.0	2.4	0.3	1.5	0.2
3PS-11-550		5.5	0.05	18.5	4.9	3.9	12.4	1.6	0.2	1.8	0.2	1.0	4.46	0.2	0.4	0.0	0.2	0.0
D2B-TS		0.1	0.11	46.7	19.6	9.4	32.2	4.0	0.9	5.2	0.2	2.2	13.41	0.4	0.9	0.1	0.5	0.1
D2B-150 A		1.5	0.15	58.1	21.7	14.4	52.5	6.8	1.6	7.7	0.6	3.4	19.70	0.6	1.3	0.1	0.7	0.1
D2B-150B		1.6	0.24	92.0	40.4	25.6	102.1	16.4	4.4	17.1	1.8	9.1	48.72	1.6	3.9	0.5	2.4	0.4
D2B-180		1.8	0.22	88.5	44.7	22.4	84.9	11.6	2.9	13.9	1.2	6.1	35.97	1.1	2.5	0.3	1.4	0.2
D2B-210		2.1	0.05	58.2	13.0	18.2	74.0	10.6	2.7	10.3	0.9	5.2	30.81	0.9	2.0	0.2	1.0	0.2
D2B-300		3.0	0.10	8.5	7.8	2.7	11.1	1.8	0.5	2.6	0.2	1.3	9.10	0.2	0.6	0.1	0.3	0.05
D2B-390		3.9	0.06	10.1	11.5	3.0	11.6	1.7	0.4	2.7	0.3	1.2	7.25	0.2	0.5	0.1	0.3	0.05
D2B-BR		5.0	0.04	6.7	3.7	1.0	3.2	0.4	0.1	0.7	0.1	0.2	1.10	0.0	0.1	0.0	0.1	0.01

NA - not analysed.

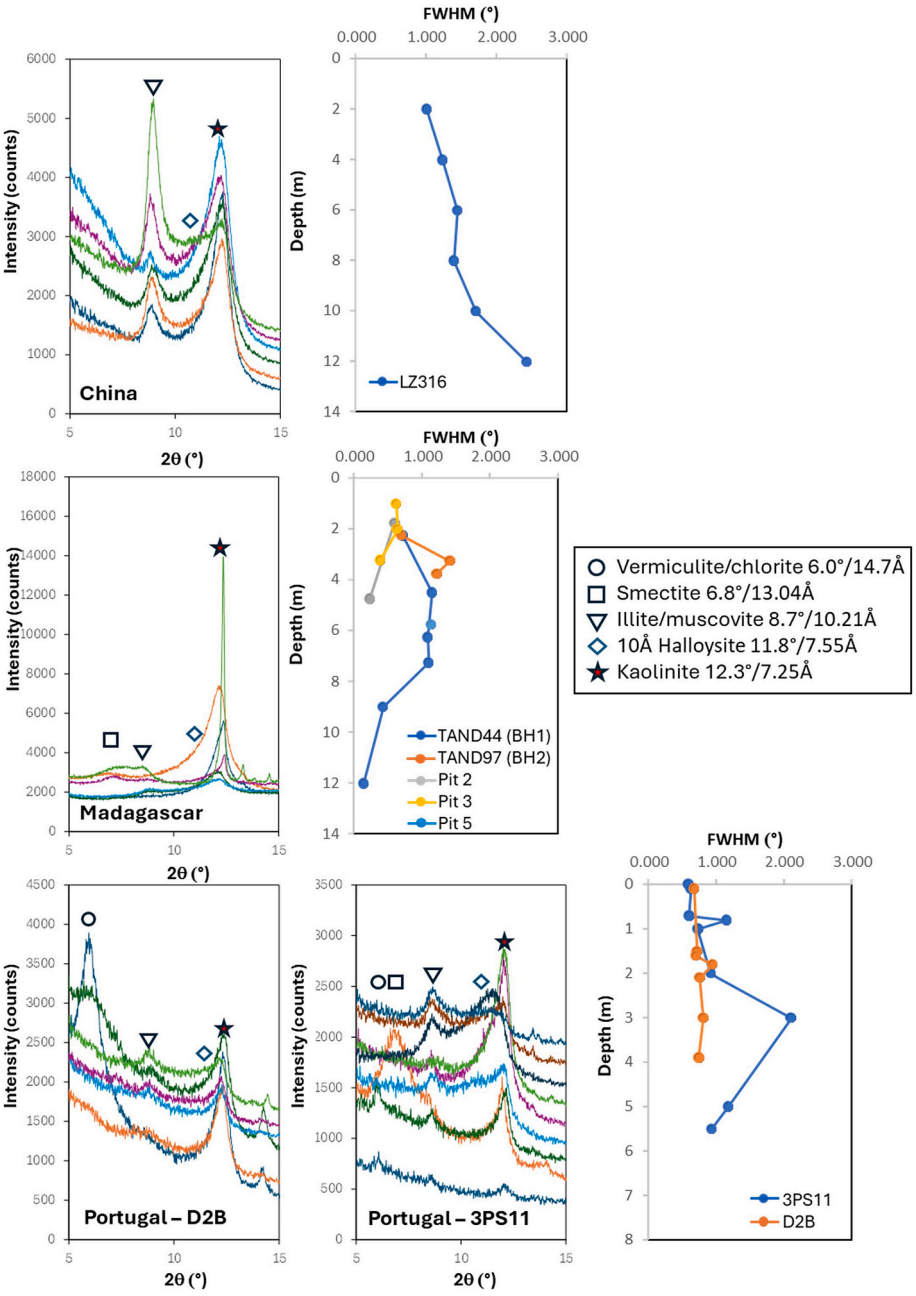

Fig. 6. X-ray diffraction patterns of oriented clay samples from 5 to 15° 2 theta, and the change in the kaolinite 7 Å peak FWHM with depth.

samples, however these samples represent winter, wet season sampling and are inferred to be the result of circulation deep into bedrock and are therefore not implicated in the formation of weathering profiles.

Modal kaolinite $\delta^{18}O$ equilibration temperatures for China and Madagascar are 32 °C and 33 °C respectively, which are comparable to the mean monthly peak temperatures of 27.8 to 29.5 °C, although shifted to slightly higher temperatures. The shift is within the range of uncertainty in the estimates. For these sites, this is consistent with the generation of kaolinite by weathering during the warm, rainy season, when both temperatures and precipitation are highest. The modal kaolinite $\delta^{18}O$ equilibration temperature for Portugal is 37 °C. This is comparable to thermal spring water discharge, and alongside the full range of temperature from 40 to 80 °C or more suggesting significant kaolinite genesis during geothermal related alteration, with a weathering overprint in some samples. At Madagascar higher temperatures (up to 80 °C) are recorded from kaolinite at depth below ~8 m, indicating that there may have been initial generation of hydrothermal kaolinite subsequently overprinted by weathering kaolinite.

4.2. *Influence of genetic conditions on kaolinite crystallinity and REE adsorption*

The temperature of formation is a key influence on the grain size and crystallinity of the resulting kaolinite (Mahmoud et al., 2018). Other factors include aqueous transport and the pH and salinity of formation, transport and depositional solutions (Hinckley, 1965; Mahmoud et al., 2018; Ishida et al., 2018). Ishida et al. (2018) proposed a model for weathering genesis of kaolinite in podzol profiles, in which kaolinite dissolution at pH ~4 in the upper profile reduces the proportion of reactive, poorly crystalline kaolinite, with subsequent precipitation of high-defect, poorly crystalline kaolinite at higher pH (4.5–6). These processes are clearly represented in the Zhaibei profile, where the

Table 4
X-ray diffraction characteristics of the kaolinite 7 Å peak, with the calculated mean crystallite size using the Scherrer equation.

	FWHM (°2θ)	Peak position (°2θ)	d (Å)	Intensity	Crystallite size (nm)
Madagascar - Ambohimirahavavy					
SR211	0.71	12.36	7.19	3724	11.69
Sr220	1.14	12.17	7.31	4890	7.30
SR227	1.08	12.06	7.37	1144	7.73
SR231	1.10	12.17	7.31	639	7.62
SR238	0.42	12.40	7.17	1493	19.69
SR246	0.14	12.36	7.20	11,404	61.39
SR275	0.70	12.07	7.37	2994	11.99
SR279	1.41	11.88	7.48	387.5	5.93
SR306	1.21	12.04	7.39	1528	6.89
SR573	1.13	12.04	7.38	2322	7.4
SR586	0.59	12.22	7.28	11,878	14.08
SR597	0.23	12.28	7.24	22,722	36.94
SR611	0.61	12.30	7.23	11,745	13.69
SR617	0.64	12.10	7.35	14,048	13.14
SR624	0.38	11.76	7.56	3339	21.96
China - Zhaibei					
LJ316–2	1.01	12.24	7.48	2091	8.26
LJ316–4	1.23	12.24	7.48	1400	6.77
LJ316–6	1.45	12.22	7.49	1621	5.77
LJ316–8	1.40	12.21	7.50	2065	5.98
LJ316–10	1.71	12.21	7.50	1689	4.89
LJ316–12	2.43	12.30	7.44	982	3.44
Portugal - Monchique					
3PS-11-OX	0.59	11.94	7.41	513	14.15
3PS-11-TS	0.63	12.12	7.29	51	13.25
3PS-11-70	0.60	12.12	7.30	362	13.91
3PS-11-80	1.15	11.99	7.37	728	7.26
3PS-11–100	0.73	12.02	7.36	1159	11.43
3PS-11-200	0.92	12.12	7.30	823	9.07
3PS-11-300	2.10	11.68	7.57	1285	3.97
3PS-11-500	1.18	12.03	7.35	275	7.07
3PS-11-550	0.93	11.48	7.70	65	8.97
D2B-TS	0.68	12.29	7.20	1040	12.28
D2B-150 A	0.72	12.27	7.21	592	11.59
D2B-150B	0.70	12.40	7.13	528	11.93
D2B-180	0.95	12.36	7.15	1123	8.79
D2B-210	0.76	12.24	7.23	347	10.98
D2B-300	0.81	12.23	7.23	399	10.31
D2B-390	0.74	12.22	7.23	207	11.28
D2B-BR Extract					

kaolinite crystallinity decreases with depth (FWHM increases). At Ambohimirahavavy and Monchique a decrease in crystallinity is observable from the upper parts of the profiles to ~4–6 m and 3–4 m respectively, but the lower profiles host better crystalline kaolinite. This is particularly notable for the oxide zone samples from Monchique, in which the highest kaolinite FWHM/crystallite size are preserved in the upper portion of the profile (Table 4).

Given the study sites are the result of in-situ weathering with similar pH environments, temperature and moisture content are key controls for the differences between sites. Fig. 9 compares the apparent temperature of kaolinite equilibration with crystallographic parameters of kaolinite (represented by the FWHM of the 12° 2θ diffraction peak), and the percentage of REE leached. The latter is also dependent on the leaching, adsorption and reprecipitation processes in the profile, and the relative proportion of Ce relative to the other REE (as in oxide zones Ce predominates over other REE as CeO_2). Data are therefore differentiated by Ce anomaly in Fig. 9 as well as by site, with leached zones identified by characteristic positive Ce-anomalies resulting from Ce oxidation. Pearson correlation co-efficients between the variables are shown in Table 6.

Taken as a whole there is very little correlation between the %REE leached and the apparent temperature of kaolinite formation (Fig. 9a, Table 6). However, if the position in profile is accounted for by excluding oxidised and leaching zone samples using the Ce anomaly, there is a clear distinction between kaolinite generated from thermal water circulation (50–80 °C) with <30% leachable REE, and weathering kaolinite (25–40 °C) with typically >40% leachable REE (Fig.9b). The correlation between %REE leached and apparent T is significant at the 0.01 level (α) for those samples with a negative Ce anomaly. This can be linked to kaolinite crystallinity as the FWHM also correlates with apparent temperature (Fig. 9c, d) and to %REE leached (Fig. 9e, f). The correlation between FWHM and apparent T is significant at the 0.01 level in the full data set, and with % leached at the 0.05 level. Lower temperature (<40 °C) genesis and higher % leached both corresponding to broader FWHM and hence lower crystallinity kaolinite. A relationship between increased crystallite size, mode of formation and primary (in situ) versus secondary (transported) origin has been proposed for kaolinite (Zadvernyuk et al., 2021). tTe distinction between well crystalline hypogene kaolinite in bedrock and smaller, less crystalline, pedogenic kaolinite in saprolith has been reported from several sites (e.g. Varajao et al., 2001), the inference from this is that less well crystalline kaolinite, generated in lower temperature (>40 °C) and pH (<6) conditions, has higher surface area and proportion of adsorption sites compared to more crystalline kaolinite generated from thermal waters. Weathering genesis is critical in forming IADs in terms of producing kaolinite-rich deposits capable of hosting >50% leachable REE. There may also be an influence from bedrock protolith, particularly at Ambohimirahavavy where syenite and alkali granite dykes intrude mudstone (Estrade et al., 2019; Marquis et al., 2023). However, in samples where a mudstone protolith can be identified there is no significant difference with kaolinite from igneous protoliths (Table 4).

The role of crystallinity in adsorption capacity of kaolinite has been long established, with surface area and base exchange capacity increasing as the degree of crystallinity decreases (Murray and Lyons, 1959). Adsorption on kaolinite is governed by variable pH sites controlled by the distribution of terminal -OH groups on the aluminol surfaces and edge sites (Brady et al., 1998), so the first order control on adsorption of the REE in IADs is the change from acidic soil zone pH (~4) to higher pH (5–6.5) where water accumulates at hydraulic boundaries (Sanematsu and Watanabe, 2016; Estrade et al., 2019; Li et al., 2020). However, Li and Zhou (2020, 2023) showed an increase in cation exchange capacity, pore volume, and surface area with depth from upper pedolith into lower pedolith and saprolite in the Zhudong and Bangkeng deposits, South China, as well as notable decreases in kaolinite crystallinity with depth accompanying an increase in adsorbed REE at Zhudong. Trends of decreasing crystallinity with depth were attributed to the dissolution of small crystallite size, low crystallinity kaolinite preferentially to coarser kaolinite, in the upper pedolith, and reprecipitation deeper in the weathering profile as poorly crystalline kaolinite (Ishida et al., 2018). Distinction in crystallinity may be responsible for trace element variations between hypogene and supergene kaolinite; as noted in some areas where hypogene kaolinite is enriched in S, Ba and Sr, and supergene kaolinite is enriched in lanthanides (e.g. Dill et al., 1997). Halloysite has been reported from Ambohimirahavavy (Estrade et al., 2019) and Chinese deposits (Li and Zhou, 2020), but is lower in concentration than kaolinite, and would have comparable effects to those inferred here.

Additional controls on the % total REE leachable from bulk rock may arise because of the formation of inner sphere complexes on clay surfaces by desolvation of hydrated REE^{3+} complexes at alkaline pH (5.5 for Eu^{3+} adsorption on smectite and kaolinite; Stumf et al., 2002), adsorption and incorporation into metal oxides and the presence of weathering resistant relict phases from bedrock. Direct measurement of lanthanide structural site on kaolinite from IADs, including Zhaibei and

Table 5
Oxygen and hydrogen stable isotope composition of purified clay separates and waters.

Sample	Depth (cm)	$\delta^{18}O$ (‰)*	dD (‰)*	Sample	Depth (cm)	$\delta^{18}O$ (‰)*	dD (‰)*
Madagascar - Ambohimirahavavy				D2B-150 A	150	18.7	
SR211	225	18.6		D2B-150B	150		−58.6
Sr220	450	19.1	−49.8	D2B-180	180	18.9	−54.7
SR227	625	19.8	−49.8	D2B-210	210	17.3	−52.7
SR231	725	18.9	−57.6	D2B-300	300	19.4	−55.6
SR238	900	13.5	−45.4	D2B-390	390	19.4	−49
SR246	1200	10.8		D2B-BR	Bedrock	7.2	
SR275	225	21.5	−50.6	**Water samples**			
SR279	325	19.9	−36.3	**Sample**	**Location**		
SR306	375	17.2		**Madagascar - Ambohimirahavavy**			
SR573	575	20.2	−24.7	**Surface water**			
SR586	175	18.2	−41.5	SR559A	Betaimboay river	−4.4	−17.4
SR597	475	17.1	−42.8	SR560A	Pit3 groundwater	−4.4	−19.8
SR611	100	18.4	−50.6	SR561A	Pit 5 groundwater	−4.6	−22.1
SR617	200	18.4		SR610	Ankatafa river	−4.1	−19.3
SR624	325	19	−32.8	SR619	Antsirabe groundwater	−4.4	−22.4
China - Zhaibei				SR626	Antsirabe groundwater	−3.1	−18.4
LJ316–2 m	200	18.5	−62.9	SR678	Berondra river	−3.3	−17.2
LJ316–4 m	400	16.5	−55.2	SR679	Tsarabanja river	−2.9	−13.2
LJ316–6 m	600	16.8	−63	**Portugal - Monchique**			
LJ316–8 m	800	15.9	−58.6	***Pore waters***	**Depth (cm)**		
LJ316–10 m	1000	17.9	−34.1	D2B-TS	10	−2.3	−5.6
LJ316–12 m	1200	17.5	−55.9	D2B1.2 M	120	−0.7	−1.8
Portugal - Monchique				D2B-150	150	−1.4	−7.1
3PS-11-OX	Surface	18.7		D2B-270	270	0.1	3.3
3PS-11-TS	10	21.0		3PS-11-TS	10	−1.1	0.5
3PS-11-70	70	20.3		3PS-11-80	80	−1.3	4.5
3PS-11-80	80	20.4		3PS-11-70	70	−1.4	2.6
3PS-11–100	100	22.1		3PS-11-1	100	−1.1	1.7
3PS-11-200	200	23.7		3PS- 1.5	150	−1.5	−5.2
3PS-11-300	300	22.9		3PS-11-200	200	0.0	5.9
3PS-11-500	500	21.2		3PS-11-3	300	−0.3	2.7
3PS-11-550	550	21.0		3PS-11-5	500	−0.3	6.0
D2B-TS		15.6	−60	3PS-11-5.5	550	−0.4	2.7

* All values in delta notation relative to v-SMOW.

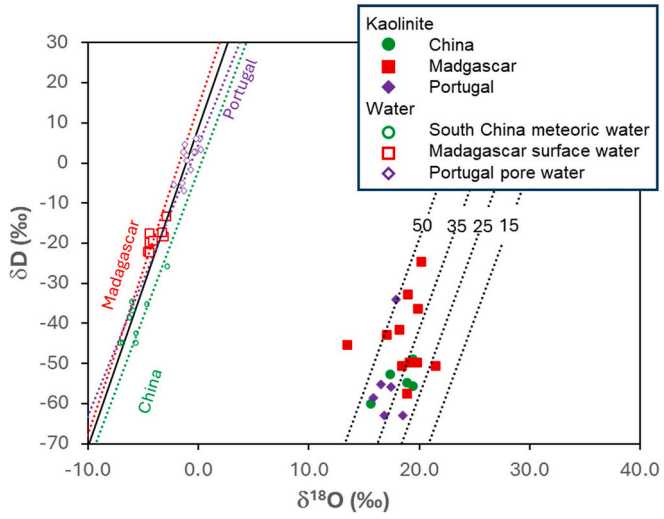

Fig. 7. The results of the oxygen and hydrogen isotope analyses of purified kaolinite separates and water samples. The data are compared to the global and local meteoric water lines (GNIP, 2024; Liu et al., 2014) and calculated kaolinite equilibration temperature using the fractionation factors of Sheppard and Gilg (1996).

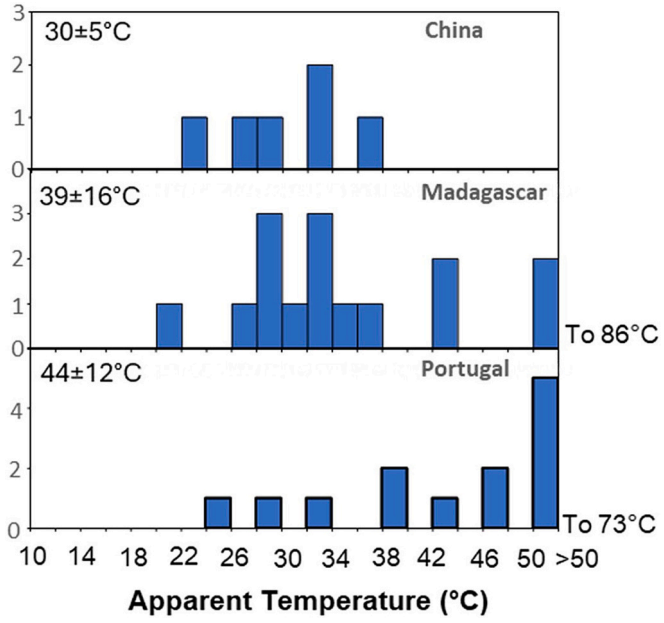

Fig. 8. Histograms of apparent equilibration temperature of kaolinite. Temperatures were calculated based on the mean local meteoric water $d^{18}O$ and the fractionation factors of Sheppard and Gilg (1996).

Ambohimirahavavy, (Yamaguchi et al., 2018; Borst et al., 2020) has only detected outer sphere complexes so inner sphere complex formation is not inferred to play a major role in variation in the % total REE leachable. Conditions where inner sphere complexation may play a major role in the REE speciation are not achieved until well below the water table (pH up to 8.5 noted in groundwaters; Li et al., 2019; Zhao et al., 2022). Where sequential leach techniques have been applied to IADs the iron oxide associated fraction is 1–10% of the clay adsorbed portion of all REE except for Ce (e.g. Li et al., 2019). Oxide incorporation may, therefore, be responsible for the spread of data but is only a minor

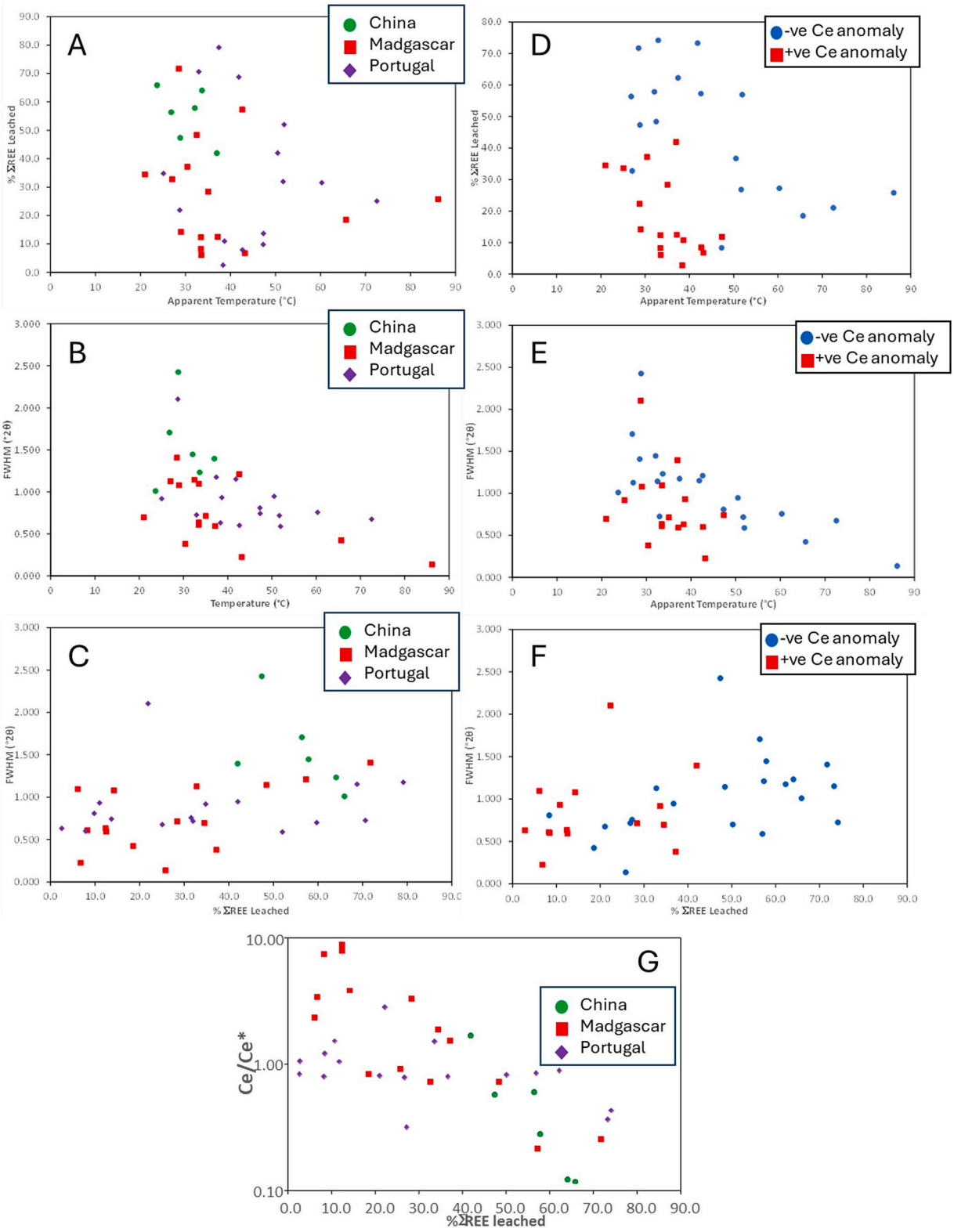

Fig. 9. Correlation of apparent equilibration temperature, mineralogy and geochemistry. (A) Temperature and % SREE leached, (B) Temperature and Kaolinite 7 Å peak FWHM. (C) % SREE leached and Kaolinite 7 Å peak FWHM, plotted subdivided by sample site (A-C) and Ce anomaly (D-F). (G) % SREE leached and Ce anomaly.

factor in the correlations shown in Fig. 9. The presence of alteration and weathering resistant phases clearly does also influence the proportion of leachable REE (e.g. Estrade et al., 2019) again influencing the spread of data in Fig. 9, but Marquis et al. (2023) noted that despite high concentrations in weathering resistant zircon-silicate minerals, the majority of the REE deportment of source igneous rocks is hosted as trace elements in weathering susceptible mafic silicates, and hence is mobilised during weathering and available for adsorption.

Based on this study and previous work, a general model from IAD formation incorporating pre-weathering hydrothermal alteration,

Table 6
Pearson correlation co-efficients for % REE leached, Ce anomaly (Ce/Ce*), Full Width Half Maximum of the Kaolinite7Å peak and formation temperature derived from isotopic data. Significant correlations in bold.

Full Data Set					
		% Leached	Ce/Ce*	FWHM (°)	T (°C)
% Leached	Pearson Correlation	–			
Ce/Ce*	Pearson Correlation	**−0.488****	–		
	Sig. (2-tailed)	0.002			
FWHM (°)	Pearson Correlation	**0.404***	−0.24	–	
	Sig. (2-tailed)	0.013	0.153		
T (°C)	Pearson Correlation	−0.243	−0.179	**−0.485****	–
	Sig. (2-tailed)	0.154	0.297	0.003	
Negative Ce/Ce*					
		% Leached	**Ce/Ce***	**FWHM (°)**	**T (°C)**
% Leached	Pearson Correlation	–			
Ce/Ce*	Pearson Correlation	**−0.592****	–		
	Sig. (2-tailed)	0.005			
FWHM (°)	Pearson Correlation	0.369	−0.326	–	
	Sig. (2-tailed)	0.11	0.161		
T (°C)	Pearson Correlation	**−0.651****	0.437	**−0.667****	–
	Sig. (2-tailed)	0.003	0.061	0.002	
Positive Ce/Ce*					
		% Leached	**Ce/Ce***	**FWHM (°)**	**T (°C)**
% Leached	Pearson Correlation	–			
Ce/Ce*	Pearson Correlation	−0.295	–		
	Sig. (2-tailed)	0.251			
FWHM (°)	Pearson Correlation	0.17	−0.082	–	
	Sig. (2-tailed)	0.515	0.753		
T (°C)	Pearson Correlation	−0.121	−0.226	−0.448	–
	Sig. (2-tailed)	0.644	0.384	0.071	

** Correlation is significant at the 0.01 level (2-tailed).
* Correlation is significant at the 0.05 level (2-tailed).

climate and weathering processes with depth can be proposed (Fig. 10). The REE are released by breakdown of REE minerals (Li et al., 2022) and REE-bearing silicates (Marquis et al., 2023), and desorption from clays in the soil zone at low pH (~4), and at topographic highs where flow is diverted laterally downslope (Estrade et al., 2019; Li et al., 2020). Kaolinite generated within this zone is relatively well crystalline because of dissolution and transport of fine grained, poorly crystalline kaolinite to deeper in the profile, alongside leaching of the REE by acidic groundwater (Sanematsu and Watanabe, 2016; Marquis et al., 2023) at pH around 4 (Ishida et al., 2018). Consequently, kaolinite within this zone is typically well crystalline, has low percentage REE and a positive Ce anomaly from arising from oxidation (Fig. 10a).

In climates with wet warm seasons, kaolinite is redeposited in saprolite as fine grained, poorly crystalline kaolinite, alongside in-situ kaolinite generation (Ishida et al., 2018). As pH changes from ~4 to 5 to 6.5 (Sanematsu and Watanabe, 2016; Ishida et al., 2018; Li et al., 2020), re-adsorption of the REE results in up to 70% leachable REE content (Fig. 10b). Experimental data (Villanova-de-Benavent et al., 2026) demonstrate a factor of 10× more adsorption on poorly crystalline kaolinite (crystallite size ~10 nm) compared to well crystallised kaolinite (crystallite size 100 nm). This is comparable in magnitude to the difference in distribution co-efficient between kaolinite of constant crystallinity and solution at pH 4 and pH 6 (Coppin et al., 2002; Villanova-de-Benavent et al., 2026). The temperature and pedogenic process controlled variations in kaolinite crystallinity inferred in this study are therefore an equally important part of the chemical trap for REE adsorption as the changes in pH with depth in weathering profiles and at hydraulic boundaries. A negative Ce anomaly is generated as a result of Ce oxidation and retention in the soil zone.

In climates with dry warm seasons, a lower extent of weathering is generated, with less marked negative Ce anomaly (Fig. 10c) in the upper soil profile. This can be tracked using bulk rock geochemical techniques such as the chemical index of alteration (CIA – Nesbitt and Young, 1984; Li et al., 2019) although this will combine effects from both hydrothermal alteration and weathering. Overprint of weathering on late epithermal kaolinite generated from thermal waters generates a range of kaolinite crystallinity. Kaolinite tends to be coarser and relatively well crystalline, presevered from alteration by thermal waters. This results in a low leachable proportion of REE. Epithermal kaolinite with low sorption capacity may also be preserved in saprock and bed rock of subtropical deposits.

4.3. Implications

The results presented here clearly indicate the role of kaolinite crystallinity in IAD formation and allow identification of factors that influence crystallinity within the genetic environment. Crystallinity is influenced both by the temperature conditions for formation (as indicated by stable isotopes), and regolith zone and associated variations in pH and redox conditions (as indicated by the Ce anomaly). This interplay of factors can result in shallow soils being rich in well-crystalline kaolinite due to leaching of reactive, poorly crystalline kaolinite. This poorly crystalline kaolinite can then be reprecipitated at as pH increases at depth. Crystallinity is thus an important input into genetic models, and clear mineralogical criteria to guide exploration for IAD occurrences. Kaolinite crystallinity can be determined from multi- and hyperspectral remote sensing data, used in both core scanning and drone mapping approaches. Kaolinite crystallinity has been evaluated from near infra-red spectra using variations in the Al-OH 4500 and 7000 cm^{-1} absorption bands (e.g. Madejová, 2003; Pineau et al., 2022). Such an approach could clearly differentiate the different kaolinite types identified here. Differentiating epigenetic from supergene kaolinite should be a target for IAD exploration and deposit evaluation, especially if combined with soil geochemistry to account for the variation in crystallinity with weathering processes and the key role of pH in REE adsorption. Hydrothermal alteration of granitoid protoliths has been

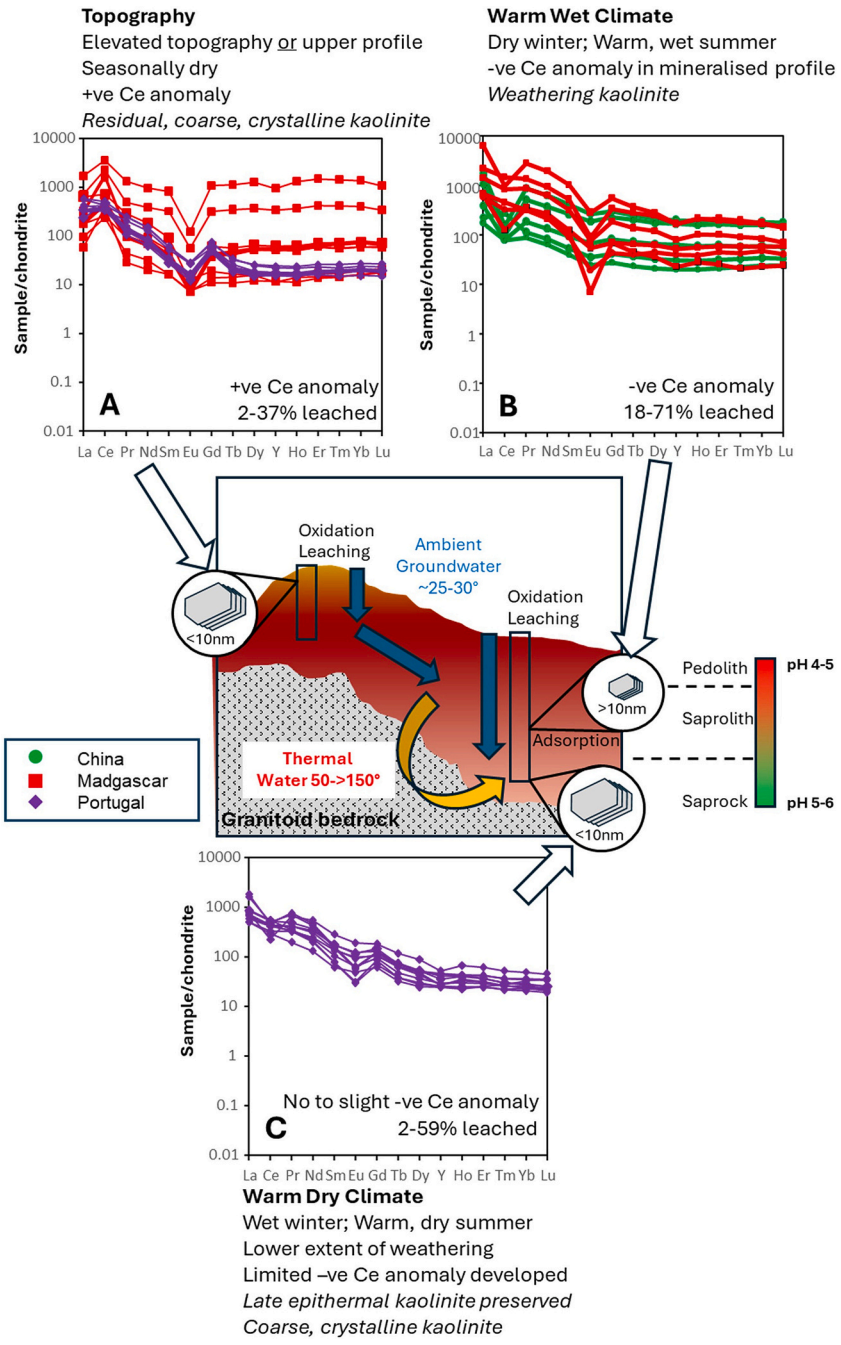

Fig. 10. Model of IAD formation processes accounting for the kaolinite genetic conditions. (A) Chondrite normalised REE patterns for upper profile and high elevation leaching zone with relatively well crystalline kaolinite. (B) Chondrite normalised REE patterns for REE adsorption in intense weathering areas (tropical and sub-tropical wet temperate climates), deeper in weathering profiles with poorly crystalline kaolinite. (C) Chondrite normalised REE patterns for REE adsorption in less intensely weathered areas with preservation of well crystalline kaolinite generated by alteration by hydrothermal waters.

identified as a key stage in IAD genesis by multiple authors, as it serves to generate more soluble REE phases (carbonates and fluorcarbonates) and precondition silicate minerals for breakdown in weathering, resulting in higher REE mobility (Li et al., 2019; Sanematsu et al., 2015; Bern et al., 2017; Marquis et al., 2023; Sanematsu et al., 2016). Such processes will also generate kaolinite, typically of a higher crystallinity than that of weathering kaolinite. Conditions of kaolinite formation are therefore a key criterion in evaluation of weathering profiles for IAD mineralisation and should be accounted for in genetic models, exploration programmes and mineral processing designs.

Equally, although ionic REE adsorption onto kaolinite has been reported from weathered rock in a range of climatic zones, it is clear from the data presented here that simple consideration of average annual temperature cannot be used to identify the most prospective areas. The enhanced weathering environment resulting in IADs is a function of both temperature and water availability, hence the most prospective areas in Holocene weathering profiles are tropical or temperate, wet summer climates (Sanematsu and Watanabe, 2016; Bao and Zhao, 2008). Similar mean annual temperatures with dry summers will not result in the same weathering extent, REE mobilisation and adsorption, as identified here for Monchique, Portugal. As, although ionic adsorption of the REE onto kaolinite clearly occurs, it is not as developed as that observed in tropical or wet temperate conditions (i.e., Zhaibei, Ambohimirahavavy). In general, favourable conditions are humid tropical to temperate climates

or paleo-climates (e.g. Zhang et al., 2023). Climates with very high rainfall may also have a negative impact on IAD preservation by causing clay dissolution and saprolite collapse (Russo et al., 2025).

The duration and timing of weathering has not been investigated here and remains a priority area for future investigations of IAD genesis. However, none of the profiles investigated here are geologically old and all inferred to still be undergoing active weathering, so the start of weathering is unlikely to be pre-Holocene. However, this study has utilized modern climate data for comparison and so does not consider change in climate through the duration of weathering. Finally, outside of fully tropical regions, seasonality clearly has a role to play in the weathering profile development. However, this variation is obscured by use of bulk kaolinite separates and mean meteoric water compositions to estimate kaolinite formation temperature.

5. Conclusions

Adsorption of REE onto kaolinite mineral surfaces as a process can occur across a range of weathering climatic conditions. This study presents data from the Monchique syenite, Portugal, the Ambohimirahavavy alkaline complex, Madagascar and the Zhaibei granite, China. The leachable fraction of REE from weathering materials on the Monchique syenite, Portugal, which is currently in a Mediterranean, temperate dry summer climate, is at certain levels comparable to the leachable fraction from deposits in Madagascar and S.E. China, which are currently in tropical, dry winter orsub-tropical no dry season climates respectively. All sites have zones within their weathering profiles that exceed 50% ammonium sulphate leachable REE, which is the widely accepted cut off for an IAD. However, the extent of weathering at Monchique, as indicated by the development of positive and negative Ce anomalies, is lower than the other two sites.

Oxygen and hydrogen stable isotope analyses of purified kaolinite separates from the three sites are consistent with two modes of formation of kaolinite – an early stage, formed under late hydrothermal conditions at >40 °C, and a later weathering kaolinite, formed at <40 °C. Apparent temperatures of weathering kaolinite formation are relatively consistent between sites at ~30 °C, despite variation in climatic zone, but the preservation of kaolinite generated from thermal waters is greater in Madagascar than China, and greatest in Portugal. The crystallinity of kaolinite relates to the temperature of formation and the position in the weathering profile. Crystallinity initially decreases with depth, related to the weathering process whereby low crystallinity kaolinite is preferentially dissolved and transported to deeper in the weathering profile. In Portugal and Madagascar kaolinite crystallinity then increases in the bedrock because of preservation of hydrothermal kaolinite. Different kaolinites can be identified based on the sign and magnitude of the Ce anomaly in associated bulk rock REE patterns, and the apparent temperature determined from stable isotope compositions.

The combination of kaolinite stable isotope composition and crystallinity allows us to propose an expansion on the current IAD genetic model, which has implications for exploration and processing of this deposit type. Pre-weathering hydrothermal alteration, down to relatively low temperatures (40–100 °C) may generate kaolinite, typically relatively well crystalline, with reduced adsorption capacity for the REE. Weathering processes subsequently leach reactive kaolinite in the soil zone, leading to a relative enrichment in more crystalline kaolinite. The combination of more crystalline kaolinite and the mobilisation of the REE at low pH (~4) results in net leaching of the REE, with the exception of Ce that is oxidised and retained as CeO_2. Deeper in the weathering profile poorly crystalline kaolinite is generated by mineral alteration and direct precipitation; this lower crystallinity kaolinite has a higher adsorption capacity for REE, alongside being a zone of higher pH (5–6.5). The extent of weathering, controlled by climatic factors including temperature and seasonality of rainfall, dictates the overall distribution of low crystallinity kaolinite and hence the final grade and tonnage of deposits.

CRediT authorship contribution statement

Martin Smith: Writing – original draft, Supervision, Project administration, Investigation, Funding acquisition, Data curation, Conceptualization. **Eva Marquis:** Writing – original draft, Methodology, Investigation, Formal analysis, Data curation, Conceptualization. **Liam Hardy:** Writing – review & editing, Methodology, Investigation, Conceptualization. **Adrian Boyce:** Writing – review & editing, Supervision, Resources. **Kathryn Goodenough:** Writing – review & editing, Supervision, Project administration, Investigation, Funding acquisition. **Guillaume Estrade:** Writing – review & editing, Methodology, Investigation. **Jindrich Kynicky:** Writing – review & editing, Resources, Investigation. **Cheng Xu:** Writing – review & editing, Resources, Investigation.

Funding sources

This work was supported by UKRI NERC grant funding to the project SOS:Rare (NE/M011429/1) and UKRI NERC Isotope Geoscience Facility grants IP-1693-1116 and IP-1639-0516. For the purpose of open access, the authors have applied a Creative Commons Attribution (CC BY) licence to any Author Accepted Manuscript version arising from this submission.

Declaration of competing interest

The authors declare the following financial interests/personal relationships which may be considered as potential competing interests:

Acknowledgements

We would like to thank Peter Lyons and Magdalena Grove for technical support at the University of Brighton. Field work in Madagascar was supported by Tantalus Ltd. with the help of F. Rasolonirina and R.L. Rakotoson. We would like to thank Prof. Marco Fiorentini for editorial handling and 2 anonymous reviewers for constructive comments which have helped improve this manuscript.

Appendix A. Supplementary data

Supplementary data to this article can be found online at https://doi.org/10.1016/j.chemgeo.2026.123491.

Data availability

All data used in the manuscript are available from the University of Brighton Research Data archive.

References

A Rocha, 2026. Profiling Portugal - the Serra de Monchique. A Rocha. Accessed 22/4/2026.

Awad, M.E., López-Galindo, A., Sánchez-Espejo, R., Sainz-Díaz, C.I., El-Rahmany, M.M., Viseras, C., 2018. Crystallite size as a function of kaolinite structural order-disorder and kaolin chemical variability: sedimentological implications. Appl. Clay Sci. 162, 261–267. https://doi.org/10.1016/j.clay.2018.06.027.

Ballinger, B., Schmeda-Lopez, D., Kefford, B., Parkinson, B., Stringer, M., Greig, C., Smart, S., 2020. The vulnerability of electric-vehicle and wind-turbine supply chains to the supply of rare-earth elements in a 2-degree scenario. Sustainable Prod. Consumption 22, 68–76. https://doi.org/10.1016/j.spc.2020.02.005.

Bao, Z., Zhao, Z., 2008. Geochemistry of mineralization with exchangeable REY in the weathering crusts of granitic rocks in South China. Ore Geol. Rev. 33, 519–535. https://doi.org/10.1016/j.oregeorev.2007.03.005.

Barbosa, S., Dias, A., Durão, D., Grilo, J., Baptista, G., Cagiza, J., Pessangam, S., Simão, J., Almeida, J., 2022. Exploring High-Resolution Chemical distribution Maps of Incompatible and Scarce Metals in a Nepheline Syenite from the Massif of "Serra de Monchique" (Portugal, Iberian Peninsula). Minerals 12, 1178. https://doi.org/10.3390/min12091178.

Beard, C.D., Marquis, E., Smith, M.P., Li, M.Y.H., Estrade, G., Goodenough, K.M., 2025. Ion adsorption mineralisation in regolith-hosted REE deposits. In: Bowell, R.J., Butt, C.R.M. (Eds.), Geology, Geochemistry and Formation of Supergene Mineral

Deposits in Deeply Weathered Terrain. Mineral Resources Reviews. Springer, Cham. https://doi.org/10.1007/978-3-031-75733-4_14.
Beck, H.E., Zimmermann, N.E., McVicar, T.R., Vergopolan, N., Berg, A., Wood, E.F., 2018. Present and future Koppen-Geiger climate classification maps at 1 km resolution. Sci. Data 5, 180214. https://doi.org/10.1038/sdata.2018.214.
Bergaya, F., Lagaly, G., 2013. Purification of natural clays. In: Faïza, B., Gerhard, l. (Eds.), Developments in Clay Science. Elsevier, pp. 213–221. https://doi.org/10.1016/B978-0-08-098258-8.00008-0.
Bern, C.R., Yesavage, Y., Foley, N.K., 2017. Ion-adsorption REEs in regolith of the Liberty Hill pluton, South Carolina, USA: an effect of hydrothermal alteration. J. Geochem. Explor. 172, 29–40. https://doi.org/10.1016/j.gexplo.2016.09.009.
Borst, A., Smith, M.P., Finch, A.A., Estrade, G., Villanova-de-Benavent, C., Nason, P., Marquis, E., Horsburgh, N.J., Goodenough, K.M., Cheng, X., Kynický, J., Geraki, K., 2020. Adsorption of rare earth elements in regolith-hosted clay deposits. Nat. Comms. 11, 4386. https://doi.org/10.1038/s41467-020-17801-5.
Brady, P.V., Cygan, R.T., Nagy, K.L., 1998. Chapter 17: Surface charge and metal sorption to kaolinite. In: Jenne, E. (Ed.), Adsorption of Metals by Geomedia. Academic press, San Dieg, pp. 371–382. https://doi.org/10.1016/B978-012384245-9/50018-9.
Chaoxi, F., Cheng, X., Aiguo, S., Smith, M.P., Kynicky, J., Chunwan, W., 2023. Origin of heavy rare earth elements in highly fractionated peraluminous granites. Geochim. Cosmochim. Acta 343, 371–383. https://doi.org/10.1016/j.gca.2022.12.019.
Chi, R.A., Tian, J., 2008. Weathered Crust Elution-Deposited Rare Earth Ores, first ed. Nova Science Publishers, New York, p. 286.
Coppin, F., Berger, G., Bauer, A., Castet, S., Loubet, M., 2002. Sorption of lanthanides on smectite and kaolinite. Chem. Geol. 182, 57–68. https://doi.org/10.1016/S0009-2541(01)00283-2.
Dickens, G.R., Koelling, M., Smith, D.C., Schnieders, L., IODP Expedition 302 Scientists, 2007. Rhizon sampling of pore waters om scientific drilling expeditions: an example from the IODP Expedition 302, Arctic coring expedition (ACEX). Sci. Drill. 4, 22–25. https://doi.org/10.2204/iodp.sd.4.08.2007.
Dill, H.G., Bosse, H.R., Henning, K.H., Fricke, A., Ahrendt, H., 1997. Mineralogical and chemical variations in hypogene and supergene kaolin deposits in a mobile fold belt the Central Andes of northwestern Peru. Mineral. Deposita 32, 149–163. https://doi.org/10.1007/s001260050081.
Donnelly, T., Waldron, S., Tait, A., Dougans, J., Bearhop, S., 2001. Hydrogen isotope analysis of natural abundance and deuterium-enriched waters by reduction over chromium on-line to a dynamic dual inlet isotope-ratio mass spectrometer. Rapid Comms. Mass Spect. 15, 1297–1303. https://doi.org/10.1002/rcm.361.
Eggleton, R.A., 2001. The Regolith Glossary. *Surficial Geology, Soils and Landscapes*. Cooperative Centre for Landscape Evolution and Mineral Exploration, National Capital Printing (CRC LEME), Kensington, Australia, p. 144.
Estrade, G., Marquis, E., Smith, M., Goodenough, K., Nason, P., 2019. REE concentration processes in ion adsorption deposits: evidence from the Ambohimirahavavy alkaline complex in Madagascar. Ore Geol. Rev. 112, 103027. https://doi.org/10.1016/j.oregeorev.2019.103027.
European Union, 2024. Establishing a Framework for Ensuring a Secure and Sustainable Supply of Critical Raw Material. http://data.europa.eu/eli/reg/2024/1252/2024-05-03.
Foley, N., Ayuso, R., 2015. REE enrichment in granite-derived regolith deposits of the Southeastern United States: prospective source rocks and accumulation processes. Symposium on strategic and critical materials proceedings, British Columbia Geological Survey Paper 2015-3, 131–138. https://pubs.usgs.gov/publication/70162148.
Gao, Y., Fan, C., Xu, H., 2017. Experimental study on adsorption of rare earth elements on kaolinite and halloysite. Acta Geol. Sin. 91, 1–3. https://doi.org/10.1111/1755-6724.13196.
Gilg, H.A., Girard, J.-P., Sheppard, S.M., 2004. Conventional and less conventional techniques for hydrogen and oxygen isotope analysis of clays, associated minerals and pore waters in sediments and soils. In: De Groot, P.A. (Ed.), Handbook of Stable Isotope Techniques. Elsevier, pp. 38–61. https://doi.org/10.1016/B978-044451114-0/50004-1.
Girard, J.-P., Freyssinet, P., Chazot, G., 2000. Unravelling climatic changes from intraprofile variation in oxygen and hydrogen isotopic composition of goethite and kaolinite in laterites: an integrated study from Yaou, French Guiana. Geochim. Cosmochim. Acta 64, 409–426. https://doi.org/10.1016/S0016-7037(99)00299-9.
GNIP, 2024. Global Network of Isotopes in Precipitation (GNIP) | IAEA. https://www.iaea.org/services/networks/gnip. Accessed 30/4/2025.
Hardy, L., Smith, M.P., Moles, N., Marsellos, A., 2016. Geochemical and mineralogical controls on the distribution of rare earth elements in the laterites of Serra de Monchique, Portugal. Trans. Inst. Min. Metall. App. Earth Sci. 125 (2), 103. https://doi.org/10.1080/03717453.2016.1166630.
Hassanzadeh-Tabrizi, S., 2023. Precise calculation of crystallite size of nanomaterials: A review. J. Alloys Comps. 968, 171914. https://doi.org/10.1016/j.jallcom.2023.171914.
Hinckley, D.N., 1965. Mineralogical and chemical variations in the kaolin deposits of the coastal plain of Georgia and South Carolina. Am. Mineral. 50, 1865–1883.
Hoque, M.A., Amponsah, K.B., Blum, A., Walton, N., Dennis, P., Butler, A.P., Hugman, S., Bamberger, A., Fowler, M., 2024. (2024) the origin and water quality of spring systems in Monchique, Portugal: A focus on Long-Term sustainability and elevated sodium levels. J. Hydrol. 637, 131363. https://doi.org/10.1016/j.jhydrol.2024.131363.
Ishida, D.A., Vieira-Coelho, A.C., Melfi, A.J., Lucas, Y., Camargo, J.P.B., Montes, C.R., 2018. Influence of pedogenetic processes on the validity of kaolinite crystallinity indices: A case study of an Amazonian Ferralsol-Podzol soil system with white kaolin. Appl. Clay Sci. 162, 435–442. https://doi.org/10.1016/j.clay.2018.06.025.
Klug, H.P., Alexander, L.E., 1975. X-Ray Diffraction Procedures for Polycrystalline and Amorphous Materials. John Wiley & Sons, Inc., New York, p. 716.
Knorsch, M., Gazley, M., Ince, M., Kartal, M., Trunfull, E., Lilly, K., Kelaart, C., 2025. Characterisation of clay-hosted rare-earth element deposits in Australia: mineralogy, geochemistry and metallurgy. Aus. J. Earth Sci. 72, 1005–1024. https://doi.org/10.1080/08120099.2025.2570934.
Laveuf, C., Cornu, S., 2009. A review on the potentiality of rare earth elements to trace pedogenetic processes. Geoderma 154, 1–12. https://doi.org/10.1016/j.geoderma.2009.10.002.
Lawrence, J.R., Taylor Jr., H.P., 1972. Hydrogen and oxygen isotope systematics in weathering profiles. Geochim. Cosmochim. Acta 36, 1377–1393. https://doi.org/10.1016/0016-7037(72)90068-3.
Le Couteur, P., 2011. Geological Report on the Chambe Basin Area of Exclusive Prospeting Licence EPL 0325/11, Mulanje Massif, Southern Malawi, East Africa. Micron Geological Ltd., p. 101
Li, M.Y.H., Zhou, M.F., 2020. The role of clay minerals in formation of the regolith-hosted heavy rare earth element deposits. Am. Mineral. 105, 92–108. https://doi.org/10.2138/am-2020-7061.
Li, M.Y.H., Zhou, M.F., 2023. Physicochemical Variation of Clay Minerals and Enrichment of rare Earth elements in Regolith-hosted deposits: Exemplifcation from the Bankeng Deposit in South China. Clays Clay Mins. 71, 362–376. https://doi.org/10.1007/s42860-023-00250-8.
Li, M.Y.H., Zhou, M.-F., Williams-Jones, A.E., 2019. The Genesis of Regolith-Hosted Heavy rare Earth Element deposits: Insights from the World-Class Zudong Deposit in Jiangxi Province, South China. Econ. Geol. 114, 541–568. https://doi.org/10.5382/econgeo.4642.
Li, M.Y.H., Zhou, M.-F., Williams-Jones, A.E., 2020. Controls on the Dynamics of rare Earth elements during Subtropical Hillslope Processes and Formation of Regolith-Hosted Deposits. Econ. Geol. 115, 1097–1118. https://doi.org/10.5382/econgeo.4727.
Li, M.Y.H., Kwong, H.T., Williams-jones, A.E., Zhou, M.-F., 2022. The thermodynamics of rare earth element liberation, mobilization and supergene enrichment during groundwater-regolith interaction. Geochim. Cosmochim. Acta 330, 258–277. https://doi.org/10.1016/j.gca.2021.05.002.
Liu, J., Song, X., Yuan, G., Sun, X., Yang, L., 2014. Stable isotopic compositions of precipitation in China. Tellus Ser. B Chem. Phys. Meteorol. 66, 22567. https://doi.org/10.3402/tellusb.v66.22567.
Liu, S.-L., Fan, H.-R., Liu, X., Meng, J., Butcher, A.R., Yann, L., Yang, K.-F., Li, X.-C., 2023. Global rare earth elements projects: New developments and supply chains. Ore Geol. Rev. 157, 105428. https://doi.org/10.1016/j.oregeorev.2023.105428.
Löhr, S., Spandler, C., Balderman, A., 2024. Controls on rapid rare earth element enrichment in sediments deposited by a continental-scale river system. Geochim. Cosmochim. Acta 366, 48–64. https://doi.org/10.1016/j.gca.2023.12.012.
Madejová, J., 2003. FTIR techniques in clay mineral studies. Vib. Spectrosc. 31, 1–10. https://doi.org/10.1016/S0924-2031(02)00065-6.
Mahmoud, E.A., López-Galindo, A., Sánchez-Espejo, R., Sainz-Díaz, C.I., El-Rahmany, M. M., Viseras, C., 2018. Crystallite size as a function of kaolinite structural order-disorder and kaolin chemical variability: Sedimentological implications. Appl. Clay Sci. 162, 261–267. https://doi.org/10.1016/j.clay.2018.06.027.
Marquis, E., Goodenough, K., Smith, M.P., Estrade, G., Rasolonirina, F., Rakotoson, R.L., 2023. Developing an integrated model for understanding REE deportment of the Ampasibitika Intrusion and associated Ion Adsorption Deposits. J. Pet. 64, egad046. https://doi.org/10.1093/petrology/egad046.
Maulana, A., Sanematsu, K., Sakakibara, M., 2016. An overview on the possibility of scandium and REE occurrence in Sulawesi, Indonesia. Indonesian J. on Geosci. 3 (2), 139–147. https://doi.org/10.17014/ijog.3.2.139-147.
Mentani, T., Ohmura, T., Watanabe, Y., Urabe, T., 2010. So-called "ion-adsorption type" REE deposits found in weathered crust of ilmenite-series granite in Northern Vietnam [abs]. Geol. Soc. Am. Abs. 42, 336.
Mudd, G., Josso, P., Shaw, R., Luce, A., Singh, N., Horn, S., Bide, T., Currie, D., Elliott, H., Grant, H., Halkes, R., Idoine, N., Mitchell, C., Watkins, I., Price, F., Petavratzi, E., 2024. UK 2024 criticality assessment. British Geological Survey, p. 235. Open report, OR/24/047. https://www.ukcmic.org/reports/cmic.html.
Murray, H.H., Lyons, S.C., 1959. Further correlations of kaolinite crystallinity with chemical physical properties. Clays Clay Mins. (Nation. Conf. Clays Clay Miner.) 8, 11–17. https://doi.org/10.1346/CCMN.1959.0080104.
Nassar, N.T., Pineault, D., Allen, S.M., McCaffrey, D.M., Padilla, A.J., Brainaird, J.L., Bayani, M., Shojaeddini, E., Ryter, J.W., Lincoln, S., Alonso, E., 2025. Methodology and Technical Input for the 2025 U.S. List of Critical Minerals— Assessing the Potential Effects of Mineral Commodity Supply Chain Disruptions on the U.S. Economy. USGS Open-File Report 2025–1047. https://pubs.usgs.gov/of/2025/1047/ofr20251047.pdf.
Nesbitt, H.W., Young, G.M., 1984. Predicition of some weathering trends of plutonic and volcanic rocks based on thermodynamic and kinetic considerations. Geochim. Cosmochim. Acta 48, 1523–1534. https://doi.org/10.1016/0016-7037(84)90408-3.
Padrones, J.T., Imai, A., Takahashi, R., 2017. Geochemical behavior of rare earth elements in weathered granitic rocks in Northern Palawan, Philippines. Resour. Geol. 67 (3), 231–253. https://doi.org/10.1111/rge.12123.
Pineau, M., Mathian, M., Baron, F., Rondeau, B., Le Deit, L., Allard, T., Mangold, N., 2022. Estimating kaolinite crystallinity using near-infrared spectroscopy: Implications for geology on Earth and Mars. Am. Mineral. 107, 1453–1469. https://doi.org/10.2138/am-2022-8025.
Pinto-Ward, C., 2017. Controls on the Enrichment of the Serra Verde Rare Earth Deposit, Brazil. Unpublished PhD thesis. Imperial College London, p. 442. https://doi.org/10.25560/78794.

Rauret, G., Lopez-Sanchez, J.F., Lück, D., Yli-Halla, M., Muntau, H., Quevauviller, P., 2001. EUR-19775 – The Certification of the Extractable Contents (Mass Fractions) of cd, Cr, cu, Ni, Pb and Zn in Freshwater Sediment Following Sequential Extraction Procedure BCR-701. BCR Information Series European Commission, p. 77.

Rocha, A., Schissel, D., Sprecher, A., De Tarso, P., Goode, J., 2013. Process development for the Serra Verde weathered crust elution-deposited rare earth deposit in Brazil. In: Proceedings of the 52rd Conference of Metallurgists (COM 2013), 27th-31st October 2013 Montreal, Canada.

Rock, N.M.S., 1974. Petrology and petrogenesis of the Monchique alkaline complex, southern Portugal. J. Petrol. 19, 171–214. https://doi.org/10.1093/petrology/19.2.171.

Russo, S.C., González-Álvarez, I., Cocker, H.A., McCoy-West, A.J., 2025. The fundamentals of rare earth element ion adsorption clay deposits: A mineral systems approach for exploration. J. Geochem. Explor. 278, 107845. https://doi.org/10.1016/j.gexplo.2025.107845.

Sanematsu, K., Watanabe, Y., 2016. Characteristics and genesis of ion adsorption-type rare earth element deposits. In: Verplanck, P.L., Hitzman, M.W. (Eds.), Rev. in Econ. Geol., 18 Society of Economic Geologists, pp. 55–79. https://doi.org/10.5382/Rev.18.03.

Sanematsu, K., Murakami, H., Watanabe, Y., Duangsurigna, S., Siphandone, V., 2009. Enrichment of rare earth elements (REE) in granitic rocks and their weathered crusts in central and southern Laos. Bull. Geol. Surv. Japan 60 (11−12), 527–558. https://doi.org/10.9795/bullgsj.60.527.

Sanematsu, K., Kon, Y., Imai, A., Watanabe, K., Watanabe, Y., 2013. Geochemical and mineralogical characteristics of ion-adsorption type REE mineralization in Phuket, Thailand. Mineral. Deposita 437–451. https://doi.org/10.1007/s00126-011-0380-5.

Sanematsu, K., Kon, Y., Imai, A., 2015. Influence of phosphate on mobility and adsorption of REEs during weathering of granites in Thailand. J. Asian Earth Sci. 111, 14–30. https://doi.org/10.1016/j.jseaes.2015.05.018.

Sanematsu, K., Ejima, T., Kon, Y., Manaka, T., Zaw, K., Morita, S., Seo, Y., 2016. Fractionation of rare-earth elements during magmatic differentiation and weathering of calc-alkaline granites in southern Myanmar. Mineral. Mag. 80, 77–102. https://doi.org/10.1180/minmag.2016.080.053.

Santana, I.V., Wall, F., Botelho, N.F., 2015. Occurrence and behavior of monazite-(Ce) and xenotime-(Y) in detrital and saprolitic environments related to the Serra Dourada granite, Goiás/Tocantins State, Brazil: potential for REE deposits. J. Geochem. Explor. 155, 1–13. https://doi.org/10.1016/j.gexplo.2015.03.007.

Savin, S.M., Epstein, s., 1970. The oxygen and hydrogen isotope geochemistry of clay minerals. Geochim. Cosmochim. Acta 34, 25–42. https://doi.org/10.1016/0016-7037(70)90149-3.

Sharp, Z.D., 1990. A laser-based microanalytical method for the in situ determination of oxygen isotope ratios of silicates and oxides. Geochim. Cosmochim. Acta 54, 1353–1357. https://doi.org/10.1016/0016-7037(90)90160-M.

Sheppard, S.M.F., Gilg, H.A., 1996. Stable isotope geochemistry of clay minerals. Clay Miner. 31, 1. https://doi.org/10.1180/claymin.1996.031.1.01.

Stumf, T., Bauer, A., Coppin, F., Fanghänel, T., Kim, J.I., 2002. Inner-sphere, outer-sphere and ternary surface complexes: a TRLFS study of the sorption process of Eu (III) onto smectite and kaolinite. Radiochim. Acta 90, 345–349.

Sun, S.-S., McDonough, W.F., 1989. Chemical and isotopic systematics of oceanic basalts: implications for mantle composition and processes. Geol. Soc. Lond. Spec. Publ. 42, 313–345. https://doi.org/10.1144/gsl.sp.1989.042.01.19.

Taylor, G., Eggleton, R.A., 2001. Regolith Geology and Geomorphology. John Wiley & Sons, Chichester, UK, p. 375.

Varajao, A.F.D.C., Gilkes, R.J., Hart, R.D., 2001. The relationship between kaolinite crystal properties and the origin of materials for a Brazilian kaolinite deposit. Clays Clay Mins. 49, 44–59. https://doi.org/10.1346/CCMN.2001.0490104.

Villanova-de-Benavent, C., Smith, M.P., Lyons, P., Marquis, E., 2026. Rare earth element adsorption experiments onto kaolinite in water, NaCl, Na2SO4 and NaHCO3 solutions: implications regarding ion adsorption rare earth element deposit formation. Clay Miner. 61, 1–17. https://doi.org/10.1180/clm.2026.10021.

Vitali, F., Longstaffe, F.J., Bird, M.I., Gage, K.L., Caldwell, W.G.E., 2001. Hydrogen-isotope fractionation in aluminium hydroxides: Synthesis products versus natural samples from bauxites. Geochim. Cosmochim. Acta 65, 1391–1398. https://doi.org/10.1016/S0016-7037(00)00604-9.

Wan, Y.X., Liu, C.Q., 2005. Study on adsorption of rare earth elements by kaolinite. J. Rare Earths 23, 377–381.

Wan, Y.X., Liu, C.Q., 2006. The effect of humic acid on the adsorption of REEs on kaolin. Coll. Surf. A Physicochem. Eng. Asp. 290, 112–117. https://doi.org/10.1016/j.colsurfa.2006.05.010.

Wang, L., Cheng, X., Zheng, Z., Wenlie, S., Kynicky, J., 2015. Petrological and geochemical characteristics of Zhaibei granites in Nanling region, Southeast China: Implications for REE mineralization. Ore Geol. Rev. 64, 569–582. https://doi.org/10.1016/j.oregeorev.2014.04.004.

Weather Atlas, (2026). https://nam11.safelinks.protection.outlook.com/?url=https%3A%2F%2Fwww.weather-atlas.com%2F&data=05%7C02%7Cr.paree%40elsevier.com%7Cfdf94964a8e849a3633108deb706b7fc%7C9274ee3f94254109a27f9fb15c10675d%7C0%7C0%7C639149436666713627%7CUnknown%7CTWFpbGZsb3d8eyJFbXB0eU1hcGkiOnRydWUsIlYiOiIwLjAuMDAwMCIsIlAiOiJXaW4zMiIsIkFOIjoiTWFpbCIsIldUIjoyfQ%3D%3D%7C0%7C%7C%7C&sdata=Z%2BohEO%2FeEJM81%2FTHylxVkrzLc%2FTT1LWNanlBGYoiKJY%3D&reserved=0. Accessed 1/3/2025.

Weather and Climate, 2026.. https://nam11.safelinks.protection.outlook.com/?url=https%3A%2F%2Fweatherandclimate.com%2F&data=05%7C02%7Cr.paree%40elsevier.com%7Cfdf94964a8e849a3633108deb706b7fc%7C9274ee3f94254109a27f9fb15c10675d%7C0%7C0%7C639149436666756382%7CUnknown%7CTWFpbGZsb3d8eyJFbXB0eU1hcGkiOnRydWUsIlYiOiIwLjAuMDAwMCIsIlAiOiJXaW4zMiIsIkFOIjoiTWFpbCIsIldUIjoyfQ%3D%3D%7C0%7C%7C%7C&sdata=RJTjnIquHTiMb53xZUAITg%2BY6uh09ipwc22zj2DFghs%3D&reserved=0. Accessed 22/4/2026, Google Scholar.

Yamaguchi, A., Honda, T., Tanaka, M., Tanaka, K., Takahashi, Y., 2018. Discovery of ion-adsorption type deposits of rare earth elements (REE) in Southwest Japan with speciation of REE by extended X-ray absorption fine structure spectroscopy. Geochem. J. 52, 415–425. https://doi.org/10.2343/geochemj.2.0531.

Zadvernyuk, H., Kadoshnikov, V., Shekhunova, S., Remez, S., 2021. Particle size distribution and crystallinity as indicators of kaolinite genesis. Appl. Clay Sci. 213, 106236. https://doi.org/10.1016/j.clay.2021.106236.

Zhang, M., Gong, Z., Li, J., Pan, Y., Jin, Q., Huang, C., 2023. REE mineralization related to weathering of the late Permian Emeishan basalts. J. Geochem. Explor. 245, 107146. https://doi.org/10.1016/j.gexplo.2022.107146.

Zhao, Z., Wang, D., Bagas, L., Chen, Z., 2022. Geochemical and REE mineralogical characteristics of the Zhaibei Granite in Jiangxi Province, southern China, and a model for the genesis of ion-adsorption REE deposits. Ore Geol. Rev. 140, 104579. https://doi.org/10.1016/j.oregeorev.2021.104579.